Dissolved Mn(III) is a key redox intermediate in sediments of a seasonally euxinic coastal basin

Robin Klomp[1,2], , Olga M. Żygadłowska[2], Mike S.M. Jetten[1],
Véronique E. Oldham[3], Niels A.G.M. van Helmond[1,2], Caroline P. Slomp[1,2] and Wytze K. Lenstra[1,2]

[1]Department of Microbiology, Radboud Institute for Biological and Environmental Science, Radboud University, Heyendaalseweg 135, 6525 AJ Nijmegen, The Netherlands
[2]Department of Earth Sciences, Utrecht University, Princetonlaan 8a, 3584 CB Utrecht, The Netherlands
[3]Graduate School of Oceanography, Rhode Island University, 215 S Ferry Rd, Narragansett, RI 02882, U.S.A.

Correspondence to: Robin Klomp (robin.klomp@ru.nl)

Abstract. Manganese (Mn) is an essential micronutrient and key redox intermediate in marine systems. The role of organically complexed dissolved Mn(III) (dMn(III)-L) as an electron acceptor and donor in marine environments is still incompletely understood. Here, we use geochemical depth profiles of solutes and solids for the sediment and overlying waters and a reactive transport model to reconstruct the seasonality in sedimentary dMn(III)-L dynamics and benthic Mn release in a eutrophic, seasonally euxinic coastal basin (Lake Grevelingen, the Netherlands). Our model results suggest We find that dMn(III)-L is a major component of the dissolved Mn pool throughout the year. According to the model, Our model indicates that, when O₂ is present in the bottom water, there are three major sources of pore water dMn(III)-L, when O₂ is present in the bottom water, namely reduction of Mn oxides coupled to the oxidation of Fe(II), reduction of Mn oxides coupled to organic matter degradation and oxidation of Mn(II) with O_2. Removal of pore water dMn(III)-L is inferred to primarily takes place through reduction by dissolved Fe(II). When bottom waters are euxinic in summer, model-calculated rates of sedimentary Mn cycling decrease strongly, because of a lower supply of Mn oxides. The dMn(III)-L transformations in summer mostly involve reactions with Fe(II) and organic matter. Modelled benthic Benthic release of Mn mainly occurs as dMn(III)-L when bottom waters are oxic, as Mn(II) upon initial bottom water euxinia and as both Mn(II) and dMn(III)-L when the euxinia becomes persistent. Our model findings Our findings highlight strong interactions between the sedimentary Fe and Mn cycles. Dissolved Mn(III)-L is a relatively stable and mobile Mn species, when compared to Mn(II), and is therefore more easily transported laterally throughout the coastal zone and possibly also to open marine waters.

Keywords

Manganese dynamics, benthic flux, reactive transport modelling, micronutrient

1 Introduction

Manganese (Mn) is an essential micronutrient and is one of the most abundant transition metals in natural environments (Raven, 1990; Neretin et al., 2003)(Neretin et al., 2003, Raven, 1990). In marine systems, dissolved Mn is present as either

35   Mn(II) or Mn(III) complexed to organic ligands (dMn(III)-L) (Burdige, 1993; Luther, 2010; Madison et al., 2013). Importantly, dMn(III)-L can act as either an electron acceptor or donor and can thereby play a key role as a redox intermediate in marine sediments (Kostka et al., 1995; Trouwborst et al., 2006; Madison et al., 2013). Sediments may act as a source of both dissolved Mn(II) and dMn(III)-L to overlying waters (Oldham et al., 2019). The redox state of the dissolved Mn will determine its reactivity and mobility and thus its ultimate fate in the water column (Oldham et al., 2017a; Lenstra et al., 2020).

40   Sedimentary Mn cycling is driven by interactions between Mn and other redox sensitive compounds (Burdige, 1993). For example, reductive dissolution of Mn oxides, which leads to mobilization of dissolved Mn, can be coupled to the oxidation of organic matter (OM), hydrogen sulfide (H_2S), ferrous iron (Fe(II)) or methane (CH_4) (Postma, 1985; Burdige, 1993; Aller, 1994; Beal et al., 2009). Interactions between Mn oxide and ammonium (NH_4^+) have also been proposed (Hulth et al., 1999; Thamdrup and Dalsgaard, 2000). The occurrence of this process in marine environments is still debated, however. Dissolved

45   Mn may~~The dissolved Mn generated may~~ be in the form of Mn(II) or dMn(III)-L (Madison et al., 2013; Luther et al., 2018). Dissolved Mn(II) can precipitate as Mn-carbonate when alkalinity is high (Calvert & Pedersen, 1996; Lepland & Stevens, 1998) and can adsorb onto Mn oxide minerals (van der Zee et al., 2001).

In the presence of oxygen (O_2),O_2, for example in surface sediments in marine settings with oxygenated waters, dissolved Mn(II) and dMn(III)-L can be oxidized, forming Mn oxides. When there is little O_2 penetration into the sediment or when

50   macrofauna are present, the dissolved Mn may escape to the overlying water (Slomp et al., 1997; McManus et al., 2012; Lenstra et al., 2020). In oxic waters, dissolved Mn may oxidize to Mn oxides and settle under gravitational forcing thereby enhancing the supply of Mn oxides to the sediment (Sulu-Gambari et al., 2017; Lenstra et al., 2021a). When bottom waters are anoxic, sediments will eventually become depleted of reactive Mn oxides and dissolved Mn can accumulate in the water column (Lenz et al., 2015; Dellwig et al., 2018).

55   Part of the Mn released from the sediment could consist of dMn(III)-L (Oldham et al., 2019). Dissolved Mn(III) is highly reactive, but the complexation with organic ligands can result in a meta-stable complex (Kostka et al., 1995). The strength of the bond between Mn(III) and the ligand determines the reactivity of dMn(III)-L (Luther et al., 2015; Oldham et al., 2015, 2017b). The Mn(III)-L complex can be the dominant form of dissolved Mn in sediment pore water and in the water column (e.g. Trouwborst et al., 2006; Madison et al., 2013; Oldham et al., 2017b). Oxidation of Mn(II) and reduction of Mn(IV) are

60   suggested to occur via one-electron step transitions with dMn(III)-L as an intermediate product (Luther, 2005). Formation of dMn(III)-L has been proposed to mainly take place via reduction of Mn oxides coupled to OM degradation or oxidation of Mn(II) by O_2 (Madison et al., 2013). Other pathways that produce dMn(III)-L include reduction of Mn oxides coupled to oxidation of Fe(II) and H_2S (Madison et al., 2013). Removal of dMn(III)-L is suggested to mainly occur via oxidation by O_2 to Mn(IV) (Madison et al., 2013). Reduction of dMn(III)-L by oxidation of Fe(II), H_2S, nitrite (NO_2^-) and OM is also possible

65   (Kostka et al., 1995; Oldham et al., 2015, 2019; Karolewski et al., 2021)(Kostka et al., 1995; Oldham et al., 2015, 2019), but does not necessarily always occur (Oldham et al., 2015, 2019).

In recent years, the number of areas that experience eutrophication and deoxygenation has increased strongly (Diaz & Rosenberg, 2008; Breitburg et al., 2018). Anoxia initially stimulates benthic release of dissolved Mn, since the dissolved Mn will no longer be re-oxidized near the sediment-water interface (Pakhomova et al., 2007; Lenstra et al., 2021a). Furthermore, 70   organic carbon (C_{org}) oxidation rates and the benthic release of dissolved Mn can be positively correlated (Berelson et al., 2003; McManus et al., 2012). At present we do not know to what extent dMn(III)-L contributes to dissolved Mn released from the sediment and what processes control the redox state in which Mn leaves the sediment.

The aim of this study is to understand the effects of seasonal euxinia on dMn(III)-L dynamics. This is studied in sediments in a seasonally euxinic coastal basin (Lake Grevelingen, the Netherlands). We combine detailed sediment and pore water analyses 75   with a reactive transport model that, for the first time, includes a detailed Mn(III) cycle, to investigate the main drivers of sedimentary Mn cycling and the benthic release of Mn. Our model results suggest Our results show that dMn(III)-L is released from the sediment both when bottom waters are oxic and euxinic. Furthermore, our results highlight the importance of dissolved Fe(II) for the mobilization of Mn and release of dissolved Mn from the sediment in seasonally euxinic basins.

80   **2 Methods**

2.1 Study area

Lake Grevelingen is a coastal marine system in the south-west of the Netherlands (Fig. 1). It is a former estuary that was closed by a dam on the landward side in 1964 and a dam on the seaward side in 1971, in response to major flooding in the area. A sluice on the seaward side enables sea water exchange with the North Sea. The lake has an average depth of 5.1 m but is 85   intersected by former tidal channels with several deeper basins (Egger et al., 2016).

(a)

North Sea

Scharendijke
basin

Depth [m]

Temperature [°C]

(b)

Oxygen [μmol L⁻¹]

(c)

Feb   Apr   Jun   Aug   Oct   Dec
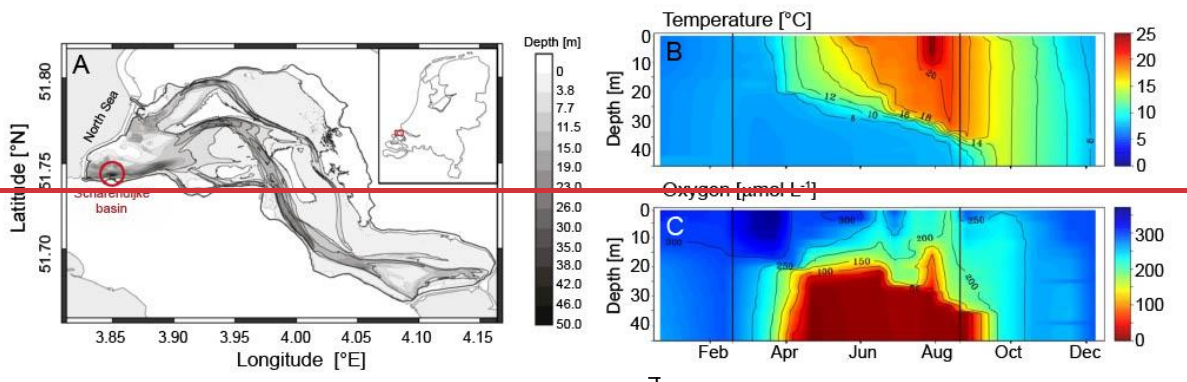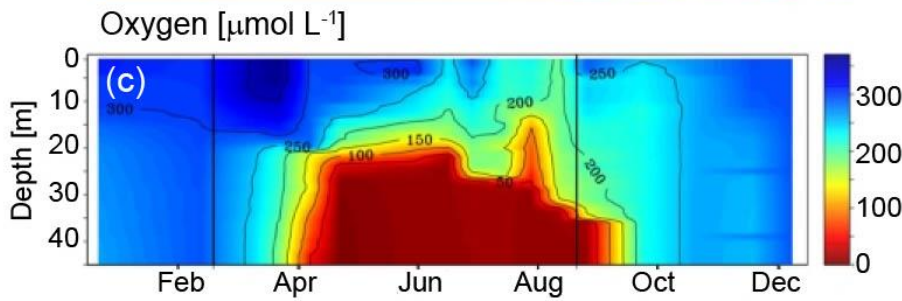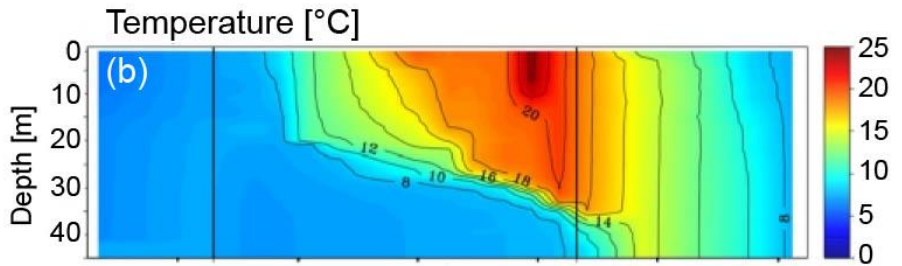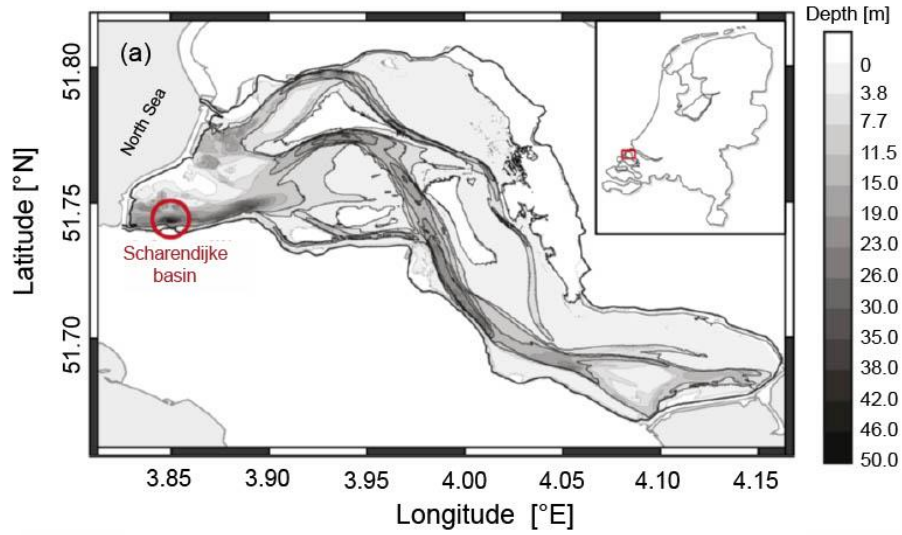
Figure 1. A) Map of Lake Grevelingen indicating the location of the Scharendijke basin (adapted from Egger et al. (2016)). B) Temperature and C) O₂ concentrations as measured by Rijkswaterstaat (Directorate-General for Public Works and Water Management of the Netherlands). The observations by Rijkswaterstaat were carried out every two weeks to one month, giving a total of 19 time points in 2020 in the water column of the Scharendijke basin throughout 2020 (Adapted from Żygadłowska et al., 2023a). The black vertical lines indicate the dates of sampling in March and September.

In this study, we focus on Scharendijke basin, located in the deepest part of the lake (Fig. 1; 51.742ºN, 3.849ºE; water depth of 45 m). During summer, temperature-driven stratification of the water column leads to the development of anoxic and sulfidic bottom waters, as recorded by the seasonal drawdown of molybdenum from the water column and its consequent sedimentary enrichment (Egger et al., 2016; Żygadłowska et al., 2023, 2024b). Water column euxinia was confirmed by direct measurements of H_2S in 2021 (Żygadłowska et al., 2024a, b). Each year, the water column mixes again in autumn, resulting in bottom water reoxygenation. Scharendijke basin is a relatively narrow and deep basin in an overall shallow lake (Figure 1). As a consequence, vertical transport settling of suspended matter is expected to be supplemented by lateral transport of material from shallower areas near the sediment-water interface. bottom water euxinia (Fig. 1; Żygadłowska et al., 2023a,b). The water column is reoxygenated in autumn. The sediment at this site is characterized by a high sedimentation rate (~13 cm yr⁻¹) and high rates of OM oxidation (~249 mmol C m⁻² d⁻¹) which is also reflected in a shallow sulfate-methane transition zone at around 20 cm depth in the sediment (Egger et al., 2016). High sulfate reduction rates lead to significant buildup of H_2S in the sediment in summer (Egger et al., 2016). Macrofauna are absent from the sediment in Scharendijke basin (based on visual observations of sediment sieved over 0.5 mm). In 2020, two (Egger et al., 2016). Two field campaigns were carried out with RV *Navicula* in 2020, one when the water column was mixed and bottom waters were oxygenated (March) and one when bottom waters were euxinic (September). During these field campaigns, the water column and sediment was sampled as described in detail below. Additional sampling was carried out in eight field campaigns, one in each month from March to October 2021, as described in the supplement (Section 1).

2.2 Water column sampling

Depth profiles of temperature and O₂ were obtained from the water column with a CTD (Seabird SBE 911 plus) equipped with an oxygen sensor (SBE43) during the cruise in September 2020. Most O₂ sensors, including the SBE43, measure a background signal when O₂ is absent. Winkler titrations can not be used for calibration, because these also have artefacts when O₂ concentrations are low (Grégoire et al., 2021). Therefore we assume absence of O₂ when oxygen concentrations are low and concentrations do not change with increasing water depth (Żygadłowska et al., 2023a). Water samples were collected with a 10 L Niskin bottle at discrete depths (1-5 m depth resolution) in September 2020. Samples were obtained for analysis of Mn(II) and dMn(III)-L and stored in a N₂ purged aluminum bag at -20°C until analysis.

2.3 Sediment and pore water collection

During both sampling campaigns in 2020, four sediment cores were collected with a UWITEC gravity corer with transparent PVC core liners of 120 cm length with a 6 cm inner diameter. During sampling, the surface sediment remained intact. The first core was sectioned for pore water and solid phase analyses at a depth resolution of 1 cm in a glove bag under a N_2 atmosphere on board the ship. The sediment was placed in 50 ml centrifuge tubes and subsequently centrifuged at 4500 rpm for 20 minutes to separate the pore water from the solid phase. Pore water was collected for all samples in the upper 10 cm, for samples from every second cm between 10 and 50 cm and every fifth cm from 50 cm until the bottom of the core. The supernatant was filtered over 0.45 μm pore size filters (i.e. capturing the aqueous and colloidal fractions; Raiswell & Canfield, 2012) under a N_2 atmosphere in a glove bag and subsequently sub-sampled for the analysis of ammonium (NH_4^+), sulfate (SO_4^{2-}), alkalinity, H_2S, total dissolved Fe and Mn and dissolved Mn(II) and dMn(III)-L. The samples for H_2S analysis were diluted five times in a 2% Zn-acetate solution in a glass vial and stored at 4°C. Samples for the analysis of NH_4^+ and, in September, for the analysis of NO_2^- and nitrate (NO_3^-) were stored at -20°C. The samples for SO_4^{2-} and alkalinity were stored at 4°C. Samples for total dissolved Fe and Mn (TD Fe and TD Mn) were acidified with 10 μL 35% suprapure HCl per ml of sample and stored at 4°C. Samples for the analysis of dissolved Mn(II) and dMn(III)-L and the sediment residues were stored in N_2 purged aluminum bags at -20°C.

The second core, with pre-drilled holes at 2.5 cm intervals covered with tape prior to coring, was used directly after retrieval to collect samples for pore water CH_4 concentrations. Plastic cut off syringes were used to transfer 10 ml of sediment directly into 65 ml glass bottles filled with saturated NaCl solution. The bottles were then stoppered, capped and stored upside down until analysis. Note that degassing of CH_4 during the sampling may lead to an underestimation of the total CH_4 concentrations, especially when CH_4 concentrations are high (Egger et al., 2017; Jørgensen et al., 2019). The third core was sectioned at a resolution of 1 cm intervals to determine sediment porosity. The sediment was placed into pre-weighed 50 ml centrifuge tubes. The fourth core was used for high-resolution depth profiling of O_2 with micro-electrodes as described in Zygadłowska et al. (2023).

2.4 Chemical analysis of pore water and water column samples

Pore water NH_4^+ was analyzed spectrophotometrically with the indophenol blue method (Solórzano, 1968). Concentrations of NO_2^- and NO_3^- were measured with a Gallery™ Automated Chemistry Analyzer type 861 (Thermo Fisher Scientific; detection limit of 1 μmol L^{-1}). Concentrations of SO_4^{2-} were measured using ion chromatography (Metrohm 930 Compact IC Flex; detection limit for SO_4^{2-} of 50 μmol L^{-1}). Alkalinity was measured through titration with 0.01 M HCl, within 24 h of sampling. Samples for H_2S were determined spectrophotometrically, using an acidified solution of phenylenediamine and ferric chloride, where H_2S is the sum of S^{2-}, HS^- and H_2S (Cline, 1969). Total dissolved Fe and Mn were determined by Inductively Coupled Plasma Optical Emission Spectroscopy (ICP-OES, Perkin Elmer Avio; detection limit 0.1 μmol L^{-1} and 0.03 μmol L^{-1} for Fe

and Mn respectively). ~~Dissolved Mn(II) and dMn(III)-L were determined simultaneously via a kinetic spectrophotometric method using porphyrin, cadmium chloride and an imidazole borate buffer as described in Madison et al. (2011; detection limit of 50 nmol L^{-1} for Mn). The analysis was done in triplicate using a 1 cm pathlength quartz cuvette in a Shimadzu UV-1900i spectrophotometer.~~

Dissolved Mn(II) and dMn(III)-L concentrations were determined simultaneously via a kinetic spectrophotometric method using porphyrin, cadmium chloride and an imidazole borate buffer as described previously (Madison et al. 2011; detection limit of 1 µmol L^{-1} for Mn). The kinetics of the Mn(II) – porphyrin reaction depends on environmental characteristics such as salinity (Thibault de Chanvalon and Luther, 2019) and should therefore be determined for each site separately. Here, the kinetic constant value for Mn(II) was determined in triplicate on an aliquot of sample in which the dissolved Mn was completely reduced by adding an excess of hydroxylamine (Oldham et al., 2015; for kinetic curves of the triplicate analysis see Fig. S1). All samples were analyzed in triplicate using a 1 cm pathlength quartz cuvette in a Shimadzu UV-1900i spectrophotometer (for examples of the kinetic curves, see Fig. S2). Our analyses were all carried out under normal atmospheric conditions. Strongly bound Mn(III)-ligand complexes cannot be measured via this method (Oldham et al., 2015; Kim et al., 2022). Therefore, the difference between the sum of measured Mn(II)/Mn(III)-L and the total dissolved Mn measured by ICP-OES can be interpreted as the amount of Mn(III)-L that is bound to strong ligands.

Prior to the analysis of CH$_4$, a 10 ml N$_2$ headspace was injected in the bottle. After seven days, when equilibrium between the water and gas phase was established, CH$_4$ was measured with a Thermo Finnigan Trace^{TM} gas chromatograph (Flame Ionization Detector; limit of detection 0.02 µmol L^{-1}).

2.5 Solid phase analyses

Porosity was determined based on the weight loss upon drying the samples in an oven at 60°C. Sediment residues for the anoxic analyses were freeze-dried and subsequently ground with an agate mortar and pestle under a N$_2$ environment. For analysis of C$_{org}$ content, aliquots of ca. 300 mg of the powdered sediment were decalcified with 1 M HCl (2-step wash; Van Santvoort et al., 2002), dried, weighed and powdered. The aliquot was analyzed with an elemental analyzer (Fisons Instruments model NA 1500 NCS) and the C content was corrected for the weight loss during decalcification. The accuracy and precision of the analyses was determined based on measurements of the internationally certified soil standard IVA2. The certified value for IVA2 is 0.732 wt.% C. The mean value that was obtained in this study for IVA2 (n=24) was 0.722 wt.% C, with a standard deviation of 0.009 wt.% C. The analytical uncertainty based on duplicates (n=15) was 0.11 wt.% C for organic C.

A second aliquot (50 – 100 mg) was analyzed via a sequential extraction procedure to determine the speciation of Fe following a combination of the methods from Poulton and Canfield (2005) and Claff et al. (2010) as described by Kraal et al. (2017) ~~(combined methods of Claff et al., 2010 and Raiswell et al., 1994 as described by Kraal et al., 2012)~~ and Mn (Lenstra et al., 2021b). The extraction procedure consists of the following five steps: (1) a mixture of 0.057 M ascorbic acid, 0.17 M sodium

185 citrate and 0.6 M sodium bicarbonate, pH of 7.5, to extract Fe oxides and easily reducible Mn, (2) 1 M HCl to extract reducible crystalline Fe oxides, Fe carbonate, FeS and Mn carbonate, (3) 0.35 M acetic acid, 0.2 M Na$_3$ citrate and 50 g L^{-1} Na dithionite, pH 4.8, to extract crystalline Fe and Mn oxides, (4) 0.2 M ammonium oxalate and 0.17 M oxalic acid to extract recalcitrant Fe oxides and non-reactive Mn such as Mn associated with clay minerals, (5) 65% HNO$_3$ was used to extract pyrite and Mn associated with pyrite. Extracted Fe and Mn in step 1, 2 and 5 was measured with ICP-OES (ICP-OES, Perkin Elmer Avio;

190 detection limit 0.1 µmol L^{-1} and 0.03 µmol L^{-1} for Fe and Mn respectively). The average recovery for Fe and Mn was 106% and 100%, respectively and the average analytical uncertainty based on duplicates (n=16) was 3.2% and 2.6%, respectively. Extracted Fe in steps 2, 3 and 4 was determined spectrophotometrically using the phenanthroline method (APHA, 2005). Average analytical uncertainty based on duplicates (n=16) was < 13.4% for all fractions of the three sequential extraction procedures. Mn extracted in step 3 and 4 is not measured, because this is mainly Mn associated with clays (Lenstra et al.,

195 2021), which is not relevant in this study. The concentration of Fe oxides is assumed to be the sum of the Fe extracted in steps 1, 3 and 4. The Fe extracted in step 2 is not taken into account for Fe oxides, because a separation of Fe(II) and Fe(III) on selected samples, to separate Fe oxides from Fe(II) containing minerals like FeS and Fe carbonate, indicated that nearly all Fe in this step was present as Fe(II). The concentration of Mn oxides is assumed to be the Mn extracted in step 1 (Anschutz et al., 2005; Lenstra et al., 2021b).

200

2.6 Calculation of benthic diffusive fluxes

Diffusive fluxes of dissolved Mn across the sediment-water interface were calculated with Fick's law of diffusion, based on the gradient in total Mn concentration between the bottom water and the pore water in the upper cm of the sediment (at an average depth of 0.5 cm) by applying the formula:

205

$$J = -\varphi D_s \frac{dC}{dz} \qquad (1)$$

where J is the diffusive flux in mmol m^{-2} d^{-1}, ϕ is the porosity of the sediment, Ds is the diffusion coefficient for Mn in the sediment in m^{-2} d^{-1}, C is the concentration of Mn in µmol m^{-3} and z is the sediment depth in m. In our calculations, we assumed all Mn was present as Mn(II), The Ds for Mn(II) was corrected for temperature and salinity using the R package CRAN:

210 marelac (Soetaert et al., 2010), taking into account the tortuosity of the sediment (Boudreau, 1996).

2.6 7 Reactive transport model

A 1-dimensional reactive transport model, written in R (version 3.6.2) and modified from (Egger et al., 2016; Lenstra et al., 2018), was used to model the sedimentary Mn cycle, including the dynamics of both dissolved Mn(II) and dMn(III)-L. The
215 model, a standard multicomponent reactive transport model, is based on the principles that are outlined in, for example, Van Cappellen & Wang (1996). The modelled components include 9 solids and 12 solutes (Table S1). Solids are transported by advection (burial), while solutes are transported both by advection and molecular diffusion. The model includes 36 reactions (Table S2, S3). The reaction parameters were obtained from the literature or constrained using the model (Table S3, S4). Chemical and physical constants were calculated using the *marelac* package (Soetaert et al., 2010) and transport coefficients
220 were calculated using the *reactran* package (Soetaert & Meysman, 2012) and were, where relevant, adjusted for environmental characteristics of at the study site (Table S5). The diffusion coefficient for dMn(III)-L was set to a lower value than that of Mn(II), because the diffusive behavior of metal-ligand complexes is typically controlled by the organic ligand (Furukawa & Takahashi, 2008; Table S6).

The model describes the upper 100 cm of the sediment column, which is divided into 1000 model layers of 1 mm. The boundary
225 conditions are set at the top of the sediment and are defined as fixed concentrations for solutes and fluxes for solids (Table S7). The model was fit to the data set for 2020. In a spin up of the model, the boundary conditions were fixed until steady state was reached after 60 years, as in Egger et al. (2016). The model was then run for 20 years, in which the seasonal cycle of oxic – euxinic conditions was simulated by varying the bottom water O_2 and H_2S concentration, the influx of Fe-oxides, Mn oxides and OM and the sedimentation rate (Fig. S1 3). The key purpose of the model application was to determine the seasonality in
230 the production and removal pathways of dMn(III)-L in the sediment and estimate the rate of diffusive release of dMn(III)-L and Mn(II) to the overlying water. Here we specifically focus on the general trends in the key processes that regulate the seasonal dMn(III)-L dynamics in a eutrophic basin. As the model focusses on these general trends, the overall picture of Mn dynamics at this site will not change due to uncertainties related to, for example, the sample resolution in the top part of the sediment.

235 In the model, high rates of CH_4 production lead to an overestimation of CH_4 concentrations because CH_4 bubble formation is not included. High rates of CH_4 production led to an overestimation of CH_4 concentrations, because CH_4 bubble formation was not included in the model. Adding bubble formation would not improve our main model results regarding dMn(III)-L dynamics, however, but would increase model uncertainty. We note that a perfect model fit of the data is not expected, due to the complexity of the system and the strong seasonal variations at our study site which also vary between years. This is
240 especially true for the fit to the solid phase profiles since such variations in the reactivity and input flux of solid phases are not specifically included in the model (Table S4, S5). A detailed model description is provided in supplement section 1 2.

A sensitivity analysis was performed to investigate the response of the benthic release of dMn(III)-L and Mn(II) to variations in OM input. The input of OM was varied by a factor of 0.01 to 2, relative to the base line scenario, leading to average OM oxidation rates ranging from 0.6 to 143 mmol C m^{-2} d^{-1} in the months when bottom waters were oxygenated and 0.9 to 219

245 mmol C m^{-2} d^{-1} in months with euxinic conditions. To obtain insight in the processes controlling the transformation and benthic release of Mn, reaction rates were integrated over the upper 10 cm of the sediment.

A forward simulation of pore water and solid phase data collected during 8 sampling events, one in each month from March to October 2021, was performed to verify the model.

3 Results

3.1 Water column and pore water profiles
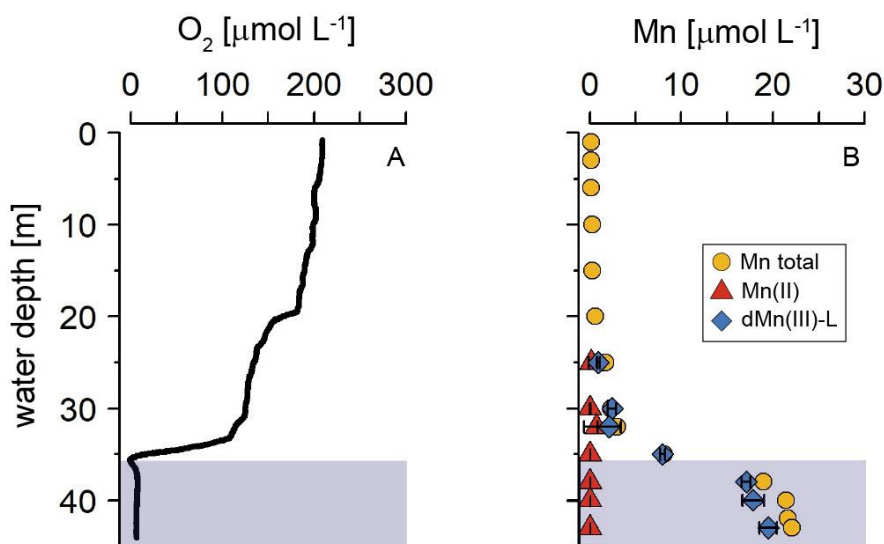
Figure 2. A) Water column O$_2$ and B) total dissolved Mn and dissolved Mn(II) and dMn(III)-L (error bars represent standard deviation; n=3) in the Scharendijke basin as observed in September 2020. The shaded area indicates the anoxic part of the water 255 column.

In March 2020, the water column of Scharendijke basin was fully oxygenated (Fig. 1). In September, in contrast, O$_2$ depletion was observed below a water depth of 35 m (Fig. 2) and dissolved Mn, primarily present as dMn(III)-L, accumulated to concentrations of up to 22 μmol L^{-1} in the anoxic waters (Fig. 2). Small enrichments in Mn(II) and dMn(III)- 260 L were observed above the redox cline at depths of 32 and 30 m, respectively.
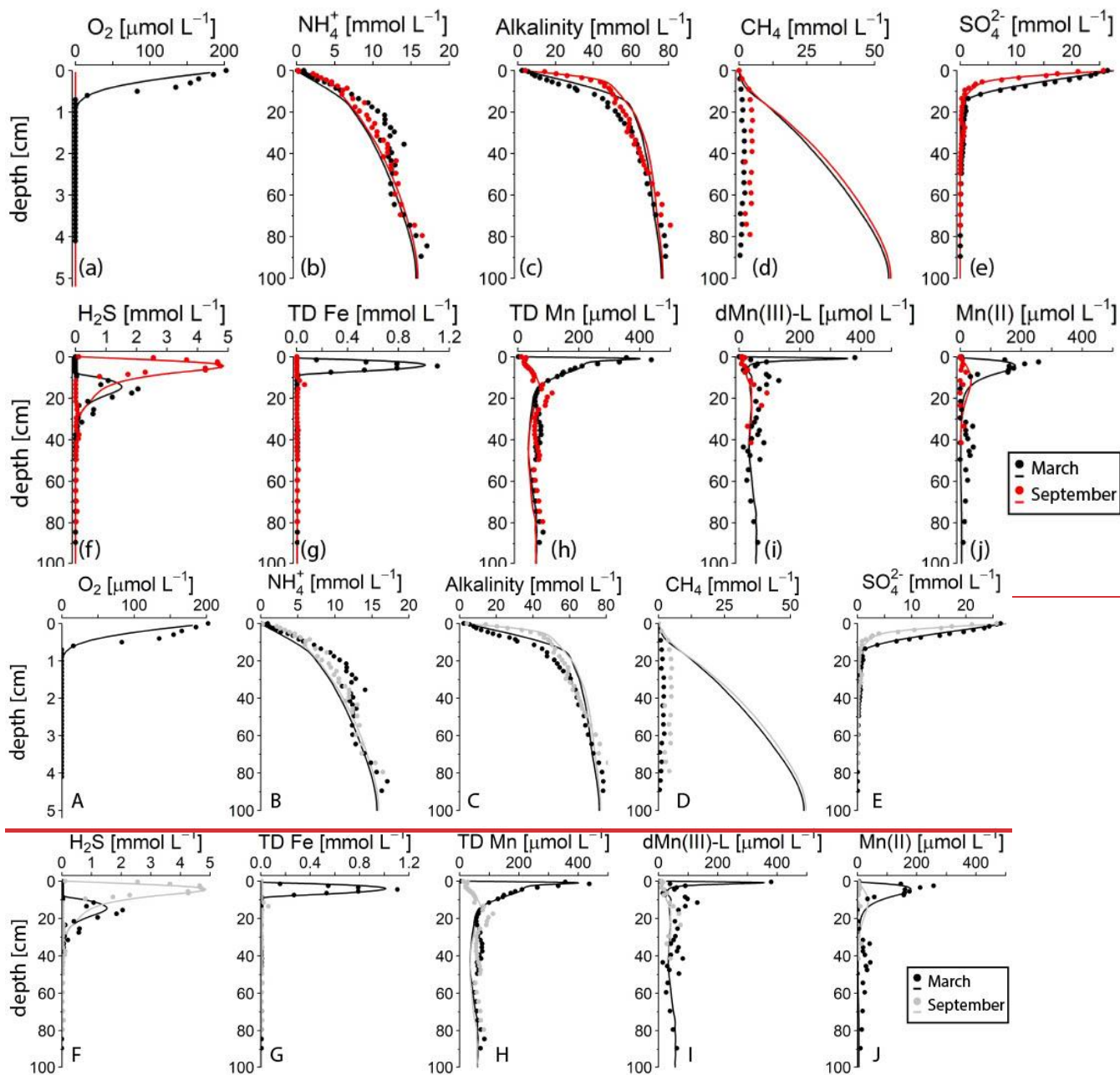
Figure 3. Pore water profiles of key components in March (black) and September (~~red~~grey) 2020. The dots represent measured concentrations, the lines indicate the results of the reactive transport model. Note the different depth scale on the y-axis for O_2. TD Fe and TD Mn refer to total dissolved Fe and total dissolved Mn. Profiles of Mn(II) and dMn(III)-L with standard deviation error bars (n =3) and the contribution to TD Mn (in %) can be found in Fig. S~~4~~2, S~~5~~3. No O_2 was detected in the sediment in September 2020. A zoom of the top 20 cm of the profiles is presented in Fig. S6.

The seasonal contrast in bottom water oxygen was reflected in the O_2 concentration in the sediment: while O_2 was present in the upper 0.6 cm of the sediment in March 2020, O_2 was absent in September 2020 (Fig. 3; for a zoom of the top 20 cm, see Fig. S6). In September, NO_2^- and NO_3^- did not exceed the detection limit of 1 µmol L^{-1} and showed no trend with depth.).

275 Concentrations of NH_4^+, alkalinity and CH_4 increased with sediment depth to maximum values of ~15, 80 and 4 mmol L^{-1}, respectively. In the surface sediment (upper 10 cm) the profiles of NH_4^+ and alkalinity showed a distinct seasonality, however, with higher concentrations in September compared to March. Profiles of SO_4^{2-} and H_2S also varied between the two seasons seasonally with SO_4^{2-} being removed at a shallower depth in September than in March and the zone of high H_2S concentrations (i.e. 1.5 to 5 mmol L^{-1}) shifting upwards by 10 cm. Dissolved Fe, in contrast, was abundantly present in the top 10 cm of the

280 sediment in March, even reaching values of up to 1.1 mmol L^{-1}, but was nearly absent from the pore water in September. Similarly, concentrations of dissolved Mn reached a maximum of 437 µmol L^{-1} near the sediment-water interface in March but were much lower in September. The peak in dissolved Mn in the upper 10 cm of the sediment in March was found to consist of two partially overlapping peaks, with that of dMn(III)-L (up to 380 µmol L^{-1}) explaining the sharp rise in dissolved Mn in the top cm of the sediment, and a broad peak in dissolved Mn(II) (up to 257 µmol L^{-1}) accounting for most (generally

285 >75%; Fig. S42) of the remaining Mn in the top 10 cm.

 Between 10 and 30 cm, dissolved Mn was mainly present as dMn(III)-L (up to 100% of the total dMn pool) and below 30 cm dissolved Mn(II) and dMn(III)-L contributed equally, both varying between 25% and 75% of the total dMn pool. In September, dissolved Mn was mainly present in the form of dMn(III)-L, which almost always accounted for >50% of the total dMn pool (Fig. S53).

290 The diffusive benthic Mn fluxes calculated with Fick's law of diffusion, based on the concentrations of the total dissolved Mn, were 2.1 mmol m^{-2} d^{-1} in March and 0.09 mmol m^{-2} d^{-1} in September.

3.2 Solid phase profiles
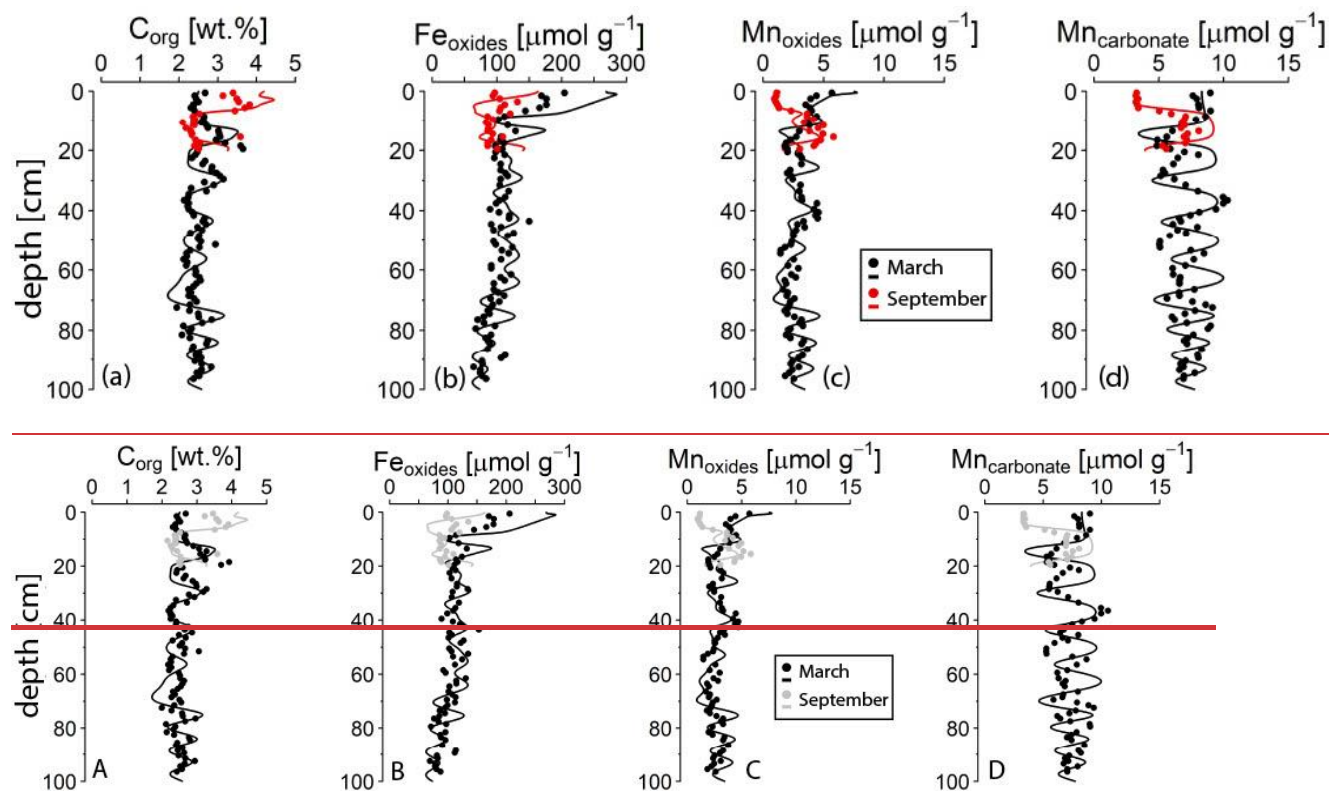
Figure 4. Solid phase profiles of key components in March (black) and September (~~grey~~red) 2020. The dots represent measured values, the lines indicate the results of the reactive transport model. Fe oxides refer to the sum of the Fe extracted in the ascorbic acid, CDB and ammonium oxalate extraction steps. Mn oxides refer to the Mn that is extracted in the ascorbic acid step. The profiles for all extraction steps are shown in Fig. S4~~7~~ and S5~~8~~.

The solid phase profiles of C_{org}, Fe- and Mn oxides and Mn carbonate reflect the strong seasonality of biogeochemical processes in the basin. ~~Concentrations of C~~org~~The C_{org} content in the top 10 cm of the sediment ~~were~~ was much lower in March 2020 (~2.5 wt%) compared to September 2020 (~3.5 wt%) (Fig. 4). In March, when O_2 was present in the bottom water, the top part of the sediment was enriched in Fe and Mn oxides and Mn carbonate. In September, when bottom waters were euxinic, surface enrichments in Fe and Mn oxides and Mn carbonate were absent (Fig. 4). The oscillations in the solid phase records are preserved upon burial of the sediment. For profiles of all the Fe and Mn fractions, we refer to the supplement (Fig. S4~~7~~, S8~~5~~). Porosity values ~~varies~~vary between 0.98 and 0.88, with a general trend towards lower values deeper in the sediment (Fig. S4~~7~~, S5~~8~~).

3.3 Sedimentary reactive transport modelling

3.3.1 Model fit

The reactive transport model generally describes the depth trends in the pore water and solid phase profiles for March and September 2020 quite well (Fig. 3, 4). For the pore water, the only exceptions are the modelled CH_4 profile and the profile of dMn(III)-L between 10 and 20 cm. ~~exception is the modelled CH_4 profile. However, given degassing of CH_4 during sampling, we cannot capture actual CH_4 concentrations at this site (Żygadłowska et al., 2023a).~~ For the solid phase profiles, the amplitude of the change in C_{org}, Fe oxide and Mn carbonate content is not always fully captured. ~~This likely results from temporal variations in the reactivity and input flux of solid phases that are not included in the model (Table S4, S5).~~ In the next sections, we will primarily focus on a description of the model results for 2020 that are relevant to dMn(III)-L dynamics.

3.3.2 Dissolved Mn(III)-L dynamics in the sediment

Rates in mmol m^{-2} d^{-1}
March / September

Influx of Mn oxides
0.81 / 0.09

Benthic flux dMn(III)-L
0.21 / 0.03

Benthic flux Mn(II)
0.01 / 0.01

Influx of Mn carbonate
0.90 / 0.17

Mn(IV) oxide

dMn(III)-L

Mn(II)

Mn carb.

dMn(III)-L + O$_2$
0.10 / 0.00

Mn(II) + O$_2$
0.29 / 0.00

Mn-ox + OM
0.30 / 0.03

dMn(III)-L + OM
0.02 / 0.00

Mn-ox + Fe(II)
0.28 / 0.01

dMn(III)-L + Fe(II)
0.55 / 0.02

Mn(II) + CO$_3^{2-}$
0.10 / 0.07

Mn-ox + H$_2$S
0.00 / 0.01

dMn(III)-L + H$_2$S
0.00 / 0.00

Mn-ox + CH$_4$
0.00 / 0.00

Flux down dMn(III)-L
0.02 / 0.01

Flux down Mn(II)
0.00 / 0.00

Burial of Mn oxides
0.36 / 0.15

Burial of Mn carbonate
0.83 / 0.37

Rates in mmol m^{-2} d^{-1}
March / September

Oxic bottom water / Euxinic bottom water

Influx of Mn oxides
0.81 / 0.09

Benthic flux dMn(III)-L
0.21 / 0.03

Benthic flux Mn(II)
0.01 / 0.01

Influx of Mn carbonate
0.90 / 0.17

Mn(IV) oxide

dMn(III)-L

Mn(II)

Mn carb.

dMn(III)-L + O$_2$
0.10 / 0.00

Mn(II) + O$_2$
0.29 / 0.00

Mn-ox + OM
0.30 / 0.03

dMn(III)-L + OM
0.02 / 0.00

Mn-ox + Fe(II)
0.28 / 0.01

dMn(III)-L + Fe(II)
0.55 / 0.02

Mn(II) + CO$_3^{2-}$
0.10 / 0.07

Mn-ox + H$_2$S
0.00 / 0.01

dMn(III)-L + H$_2$S
0.00 / 0.00

Mn-ox + CH$_4$
0.00 / 0.00

Flux down dMn(III)-L
0.02 / 0.01

Flux down Mn(II)
0.00 / 0.00

Burial of Mn oxides
0.36 / 0.15

Burial of Mn carbonate
0.83 / 0.37

325

330

335 **Figure 5. Rates of Mn cycling in March (black) and September (white) 2020 as calculated with the reactive transport model. Numbers represent depth integrated reaction rates in mmol m^{-2} d^{-1}. Note that the rates are not balanced because the system is not at steady state. The depth profiles of the reaction rates can be found in Fig. S96.**

Depth-integrated reaction rates show that, according to the model, the formation of dMn(III)-L in March 2020 is driven equally
340 by reduction of Mn oxides coupled to OM degradation and Fe(II) oxidation and oxidation of dissolved Mn(II) by O$_2$ (each
~0.3 mmol m^{-2} d^{-1}; Fig. 5; for reaction rate profiles see Fig. S96) with a negligible role for reduction of Mn oxides by H$_2$S.
Removal of dMn(III)-L in March occurs via reduction coupled to Fe(II) oxidation (0.55 mmol m^{-2} d^{-1}), oxidation by O$_2$ (0.1
mmol m^{-2} d^{-1}) and benthic release (0.21 mmol m^{-2} d^{-1}). Besides oxidation by O$_2$, dissolved Mn(II) precipitates as Mn carbonate
and is released to the water column. In September 2020, the input of Mn oxides is 9 times lower than in March, leading to
345 much lower rates of Mn cycling. Formation of dMn(III)-L is still coupled to OM degradation (0.03 mmol m^{-2} d^{-1}) and oxidation
of Fe(II) (0.01 mmol m^{-2} d^{-1}) but now oxidation of H$_2$S also contributes (0.01 mmol m^{-2} d^{-1}). Removal of dMn(III)-L in
September mainly takes place via benthic release (0.03 mmol m^{-2} d^{-1}) and reduction of dMn(III)-L coupled to oxidation of
Fe(II) (0.02 mmol m^{-2} d $^{-1}$). Again, Mn(II) is removed as Mn carbonate and via benthic release.
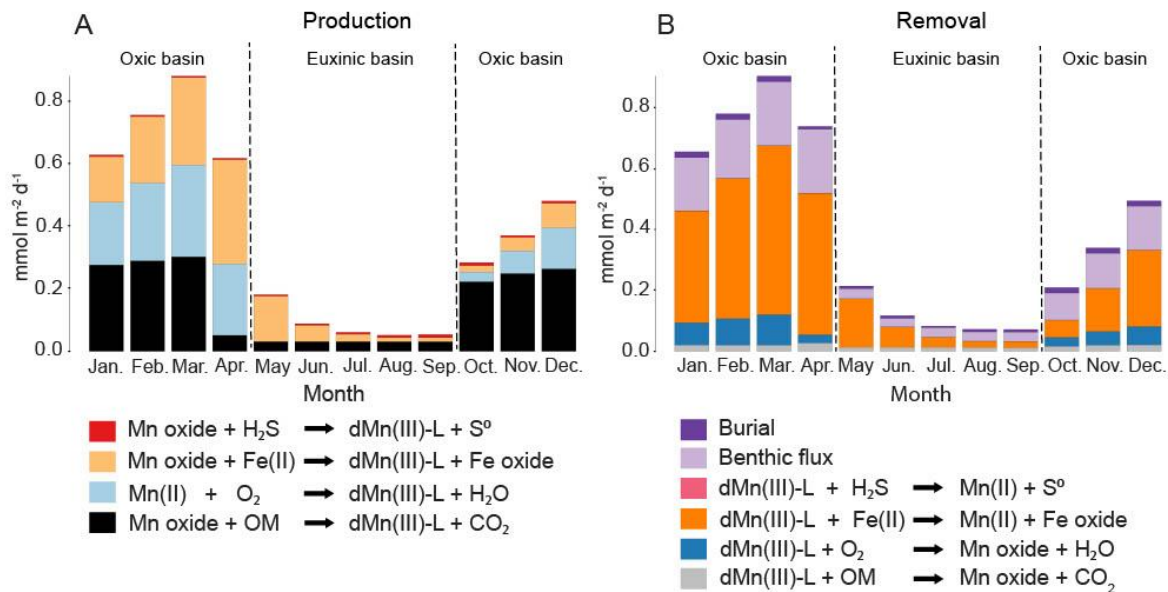
Figure 6. Depth integrated reaction rates for the sediment processes that (a) produce dMn(III)-L ~~(A)~~ and (b) that remove dMn(III)-L ~~(B),~~ as calculated with the model. The rates are calculated for each month of one year (2020) and are given in mmol m^{-2} d^{-1}.

Our model also allows us to assess trends in depth-integrated rates of dMn(III)-L production and removal in the sediment throughout the year (Fig. 6; see Fig. S~~7~~10 for modelled pore water profiles in the months between March and September 2020). Taking October as the starting point of the oxic period that lasts until April, we see that production of dMn(III)-L via reduction of Mn oxides coupled to OM degradation initially dominates. Over time, reduction of Mn oxides coupled to Fe(II) oxidation and oxidation of dissolved Mn(II) by O$_2$ become increasingly important. Following the onset of anoxia in May reduction of Mn oxides by Fe(II) becomes the major source of dMn(III)-L. During the euxinic months, the role of reduction of Mn oxide by Fe(II) decreases and OM degradation becomes the major driver of Mn oxide reduction from August onwards, followed by H$_2$S oxidation. Removal of dMn(III)-L from the sediment is dominated by reduction by dissolved Fe(II), especially during the oxic period, with additional loss through dMn(III)-L oxidation with O$_2$ (oxic period only) and benthic release.
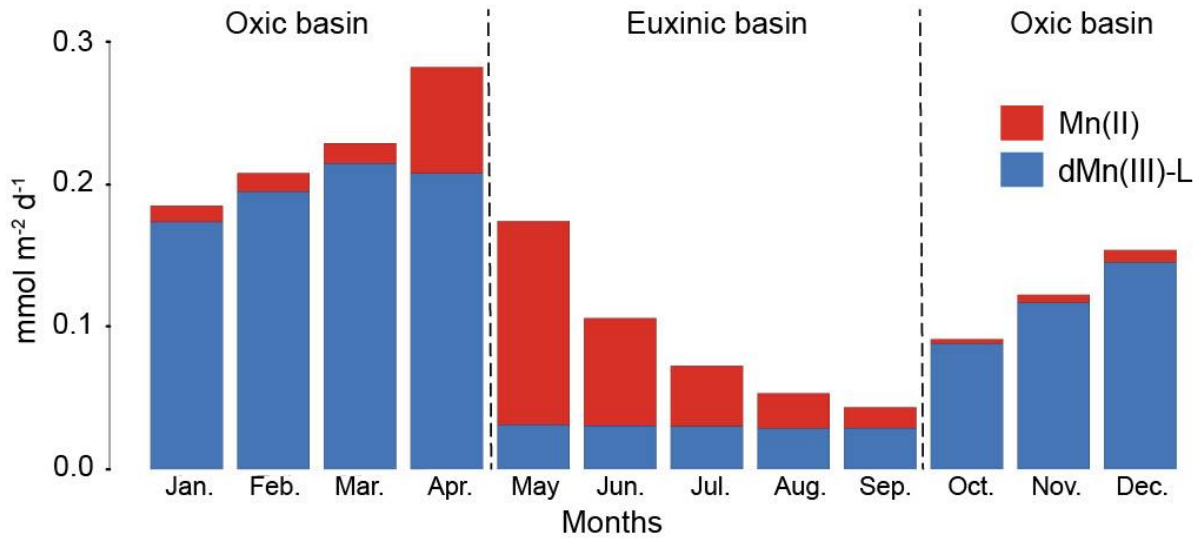
365

Figure 7. Sediment-water exchange of dissolved Mn (mmol m^{-2} d^{-1}) calculated per month in 2020. The total dissolved Mn flux consists of dissolved Mn(II) and dMn(III)-L. Positive numbers indicate a flux from the sediment to the overlying water.

According to tThe model, the benthic release of dissolved Mn is highest in the period when the bottom waters are oxic (Fig.

370   7). During this time, the flux consists primarily of dMn(III)-L. Upon the onset of euxinia in May, the flux mainly consists of Mn(II). With time, the benthic flux of Mn(II) subsequently decreases allowing the relatively constant low flux of dMn(III)-L to gain relative importance.

3.3.3 Sensitivity analysis

375
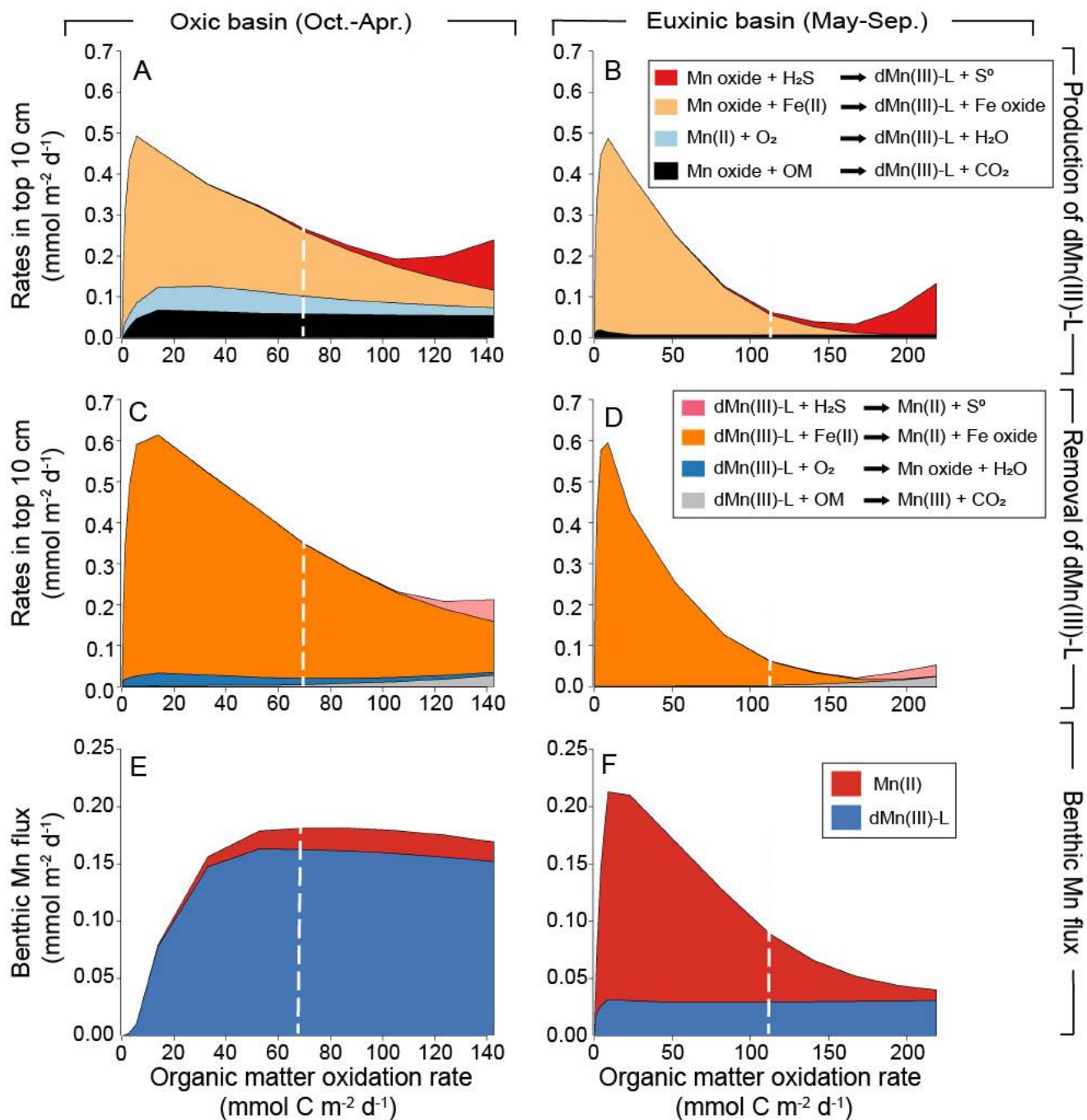
Figure 8. Depth-integrated reaction rates (0 – 10 cm) of formation (~~a~~A, ~~B~~b) and removal (~~C~~c, ~~d~~D) of dMn(III)-L as a function of rates of organic matter oxidation in the sensitivity analysis. Note that the months when the basin is oxic (October – April; ~~a~~A, ~~C~~c) and euxinic (May – September; ~~B~~b, ~~D~~d) are separated. Average benthic flux of dissolved Mn(II) and dMn(III)-L as a function of the

rate of organic matter oxidation in the months when the basin is oxic (~~Ec~~; October - April) and when the basin is euxinic (~~Ff~~; May -
September). The vertical white dashed line represents the baseline run.

To study the effect of variations in OM degradation rates on the benthic release of Mn, a model sensitivity analysis ~~was performed~~ in which the input of OM was varied was performed. The sensitivity analysis revealed that, in the model, average rates of formation and removal of dMn(III)-L for the oxic and euxinic periods are highly dependent on OM oxidation rates (Fig~~ure~~. 8). Rates of all processes involving dMn(III)-L initially increase upon a rise in OM oxidation rates and then show a variable response, either decreasing (Fe(II), O_2), remaining largely constant (OM) or increasing (H_2S). Reactions involving dissolved Fe(II) generally dominate. The role of processes involving Fe(II) diminishes, however, during the euxinic months when rates of OM oxidation are above 150 mmol m^{-2} d^{-1}.

According to the model, ~~T~~the average benthic flux of Mn during the oxic period is highly sensitive to OM oxidation rates between 0 and 50 mmol m^{-2} d^{-1} and shows a strong increase before stabilizing (~~Figure~~ Fig. 9~~8~~). Most of the Mn is released as dMn(III)-L. The pattern is different for the euxinic period: here, again an initial increase in the Mn flux is observed when OM oxidation rates vary between 0 and 10 mmol m^{-2} d^{-1}, but this is followed by a strong decrease. In this case, most of the Mn is released as Mn(II), except for the model runs with the highest OM oxidation rate: here dMn(III)-L gains importance.

3.3.4 Forward simulation

The forward simulation for 2021 using depth profiles of pore water NH_4^+, alkalinity, SO_4^{2-}, H_2S, TD Fe, TD Mn and sediment Mn oxides and Mn carbonates obtained for 2021 shows that, without any additional fitting, our model is able to capture the major trends in the sedimentary Mn cycle and key pore water constituents over a spring-summer-fall cycle (Fig. S11).

4 Discussion

4.1 Mn(III) is a key pore water component in a eutrophic coastal system

 Dissolved Mn(III)-L is frequently observed in pore waters at sites where O_2 is present in the surface sediment (Madison et al., 2011, 2013; Oldham et al., 2019). Here, we show that dMn(III)-L is also a key pore water component in a setting where O_2 is absent and bottom waters are euxinic (Fig. 3). The results of our reactive transport model suggest ~~Our reactive transport model shows~~ that the pathways of production and removal of dMn(III)-L strongly depends on the pore water composition, with Fe(II) playing a critical role.

In March 2020, when bottom waters were oxic, a maximum in dMn(III)-L was observed in the top centimeter. This maximum is based on one individual data point, but we note that it is based on triplicate analyses (Fig. S4) and is in accordance with the

peak in total dissolved Mn determined via an independent procedure (ICP-OES; Fig. S4). Additionally, such a sharp peak in

410   dMn(III)-L at the oxic/anoxic interface is expected when O_2 is involved in the production of dMn(III)-L (Madison et al., 2013). The model underestimates the dMn(III)-L concentrations between depths of 10 to 20 cm, which we attribute to an incomplete understanding of the processes that impact dMn(III)-L production and formation in sulfidic sediments. We note that the good fit of the model for most pore water and sediment components for 2020 and, as an outcome of the forward modelling, for 2021, gives confidence in the results.

415   According to the model, formation are oxic, formation of dMn(III)-L in the pore water at our site in March is driven by - at equal rates - reduction of Mn oxides by OM and Fe(II) and oxidation of dissolved Mn(II) by O_2 (Fig. 5). This contrasts with the production pathways of dMn(III)-L estimated from pore water profiles and solid phase data for different sites in the Saint Lawrence Estuary and Gulf, which pointed towards a dominant role for oxidation of Mn(II) by O_2 (Madison et al., 2013). This difference is likely due to the exceptionally large input of OM and Fe oxides at our study site, with a modelled average input

420   of ~240 mmol C m^{-2} d^{-1} and ~19 mmol reactive Fe m^{-2} d^{-1} throughout the year (Fig. S3⁠1; approximately half of the reactive Fe is accounted for by Fe extracted in ascorbic acid Fig. S7⁠4, S5⁠S8), compared to maximally 10 mmol C m^{-2} d^{-1} and 0.6 mmol Fe m^{-2} d^{-1} (Fe extracted with ascorbic acid) in the St. Lawrence Estuary and Gulf (Oldham et al., 2019).

In September 2020, when O_2 is was absent from the pore water at our site, Mn oxide concentrations in the top layer of the sediment were low compared to March. This was likely the result of a lower input of Mn oxides when the bottom water was

425   sulfidic, linked to quick reduction of Mn oxides in the water column. Under these conditions, dMn(III)-L was dMn(III)-L is mainly formed via reduction of Mn oxides by OM, with a smaller contribution of Mn oxide reduction by H_2S and Fe(II) (Fig. 5). Strikingly, dMn(III)-L co-occured⁠s with H_2S in the pore water, despite H_2S concentrations of several millimolar (Fig. 3). A co-occurrence of dMn(III)-L and H_2S was observed previously in estuarine waters at H_2S concentrations of several micromolar (Oldham et al., 2015). In this previous work, the co-occurrence was attributed to stabilization of dMn(III)-L by

430   organic ligands that kinetically hindered Mn(III) reduction by H_2S (Oldham et al., 2015). Our results suggest that stabilization of dMn(III)-L against reduction by H_2S is even possible when H_2S concentrations reach several millimolar.

According to our model, most dMn(III)-L at the study site is Most dMn(III)-L at our study site is removed through reduction by Fe(II) (Fig. 5), explaining the strong counter gradients between dMn(III)-L and dissolved Fe in March (Fig. 3; Fig S7). Apparently, the ligands that stabilize dissolved Mn(III) do not shield the Mn(III) against reduction by Fe(II). The larger role

435   of Fe(II) as a reductant for dMn(III)-L then observed in the study by Madison et al. (2013) may be explained by the approximately 20 times higher Fe(II) concentrations at our site. Previous reactive transport modelling has highlighted the role of Fe(II) in the reduction of Mn oxides (Van Cappellen & Wang, 1996). What is novel here is that dissolved Fe(II) not only plays a key role in Mn oxide reduction and dMn(III)-L production but also in dMn(III)-L removal. We note that this role of Fe(II) in dMn(III)-L dynamics came⁠omes to a halt in August and September when the Fe-oxides that accumulated in winter

440   are were completely reduced and dissolved Fe precipitate⁠sd with H_2S as FeS and FeS_2. Taken together, this indicates that, in Fe rich coastal systems, sediment Fe dynamics can be an even more important driver of Mn cycling than previously considered

(e.g. Madison et al., 2013). The results of the sensitivity analysis highlight that the role of Fe(II) in dMn(III)-L cycling holds over a wide range of OM oxidation rates (Fig. 8).

Due to its organic complexation the diffusion coefficient of dissolved Mn(III) is expected to be lower compared to that of dissolved Mn(II) (Furukawa & Takahashi, 2008; Kalinichev & Kirkpatrick, 2007). (Kalinichev and Kirkpatrick, 2007; Furukawa and Takahashi, 2008). Additionally, due to heterogeneity within the ligands that can stabilize dissolved Mn(III) (Madison et al., 2013; Oldham et al., 2015, 2017b), the diffusion coefficient of the complex of dMn(III)-L can vary per location. We find that a difference in diffusion coefficient between dMn(III)-L and Mn(II) is essential to describe the sharp gradients in the dissolved Mn profiles in the model (Fig. S8). Without a lower diffusion coefficient for dMn(III)-L it is not possible to form a sharp peak in dMn(III)-L near the sediment-water interface in our model (Fig. S12). Notably, all modelling studies of sedimentary Mn cycling to date focus only on dissolved Mn(II) excluding dMn(III)-L, which can explaining why similar sharp gradients in dissolved Mn near the sediment water interface have so far been difficult to capture (e.g. Slomp et al., 1997; Reed et al., 2011)(e.g. Reed et al., 2011; Slomp et al., 1997). The adjusted diffusion coefficient for dMn(III)-L is 16.6 cm^2 yr^{-1}, 8 times lower than the diffusion coefficient for Mn(II) (132.6 cm^{-2} yr^{-1}; Table S6). When we assume all dissolved Mn is present as Mn(II) the calculated diffusive flux of dissolved Mn would be ca. 10 and 3 times higher than when we consider both Mn(II) and dMn(III)-L in March and September, respectively. The lower diffusion coefficient of dMn(III)-L when compared to Mn(II) also implies that calculated diffusive fluxes across the sediment-water interface will be overestimated if all Mn is assumed to be present as Mn(II) (Fig. S713).

4.2 Seasonality in benthic Mn fluxes

The model results imply that throughout the year, both dissolved Mn(II) and dMn(III)-L contribute to the release of Mn from the sediment to the overlying water (Fig. 7). The flux is highest and primarily consists of dMn(III)-L under oxic conditions in winter and spring, when the input of Mn oxides and recycling of Mn near the sediment-water interface is highest. The high contribution of dMn(III)-L to the benthic Mn flux in the oxygenated basin results from faster oxidation of Mn(II) with O$_2$ compared to dMn(III)-L, which leads to a build-up of dMn(III)-L just below the sediment-water interface and subsequently a high benthic flux of dMn(III)-L.

When euxinic bottom-water conditions are established in summer, the modelled benthic flux primarily consists of Mn(II), because Mn(II) is no longer oxidized by O$_2$ (Fig. 7). However, a fraction of the Mn released from the sediment remains dMn(III)-L, indicating that a part of the dMn(III)-L released is a product of Mn oxide reduction rather than Mn(II) oxidation. As sediments become depleted in Mn oxides, typically during persistent hypoxia or anoxia, the benthic flux of Mn is known to strongly decrease (Slomp et al., 1997; Lenstra et al., 2021a). We find that the benthic flux of Mn decreases substantially as soon as the basin becomes euxinic, which likely indicates that highly reactive Mn oxides are quickly removed from the sediment when the input of Mn oxides decreases as a result of the bottom water euxinia. This is supported by the pore water and sediment data for the fieldwork campaigns between March and October in 2021 (Supplements section 1; Fig. S11). The

TD Mn in the pore water already decreases between March and April 2021 and remains low throughout the euxinic period that lasts from June to September (Żygadłowska et al., 2024b). We note that part of the dissolved Mn(II) in the pore water precipitates as Mn carbonate and hence is retained in the sediment. To visualize that both variations in Mn carbonate formation and input of Mn carbonate contribute to the seasonal variation in the sediment, a model run without Mn carbonate precipitation was performed (Fig. S14).

We also find that the modelled benthic flux of Mn decreases over summer. A new finding here is that, at the end of the anoxic period, the benthic Mn flux mainly consists of dMn(III)-L. The continuous release of dMn(III)-L from the sediment during the period of anoxia is reflected in the accumulation of dMn(III)-L in the anoxic part of the water column in September (Fig. 2). When bottom water O_2 re-establishes in October, the influx of Mn and Fe oxides, the rates of sedimentary Mn cycling and the benthic flux of Mn all increase. When in October bottom water O_2 re-establishes, the influx of Mn and Fe oxides, the rates of sedimentary Mn cycling and the benthic flux of Mn all increase. In subsequent months, the benthic flux of dMn(III)-L and the importance of Fe in Mn cycling continues to increase until just before the onset of a new euxinic period (Fig. 6, 7).

The sensitivity analysis reveals that the benthic fluxes of Mn(II) and dMn(III)-L are also dependent on the rate of OM oxidation in the sediment (Fig. 8). Nevertheless, the general patterns that emerged from the simulation for 2020, still hold: when bottom water O_2 is present, dMn(III)-L release from the sediment to the overlying water dominates over Mn(II) release. The reverse is found during the euxinic period when taken as a whole. Taken together, our results highlight that while Fe(II) dynamics play a critical role in dMn(III)-L production and removal in our Fe- and OM-rich coastal sediment, the presence of bottom water O_2 ultimately determines whether, on a yearly basis, Mn(II) or dMn(III)-L is the dominant form of Mn that escapes to the overlying water. Regardless of the bottom water redox conditions, the model always predicts some benthic release of dMn(III)-L.

4.3 Implications

Our results imply that dMn(III)-L should be considered as a potential pore water constituent when studying sedimentary Mn cycling in OM- and Fe-rich coastal sediments. When dMn(III)-L is released into anoxic waters, it can act as an oxidant and reductant, with potential implications for various redox interactions, as previously shown for anoxic water columns (e.g. Trouwborst et al., 2006; Yakushev et al., 2007; Oldham et al., 2015). When, in contrast, O_2 is present in the bottom water, dissolved Mn(II) will be readily oxidized to dMn(III)-L when it is exposed to meets O_2 near the sediment-water interface. As a consequence, dMn(III)-L is the main form in which dissolved Mn may leave the sediment (Fig. 79). The ligand stabilizing dMn(III)-L may not only slow down diffusion but is also likely to slow down the formation of solid phase Mn oxides (Sander & Koschinsky, 2011; Oldham et al., 2021). Because Mn oxides are subject to gravitational settling (e.g. Sulu-Gambari et al., 2017; Hermans et al., 2021) and dMn(III)-L is not, the dMn(III)-L is expected to be transported further away from the sedimentary source (Lenstra et al., 2020). Thus, the presence of dMn(III)-L can enhance the transport of Mn from the coastal zone to open marine waters. Additionally, the transport of trace metals that can be associated with Mn oxides, such as cobalt,

nickel and zinc, will be decoupled from that of Mn when it is primarily present as dMn(III)-L. Additionally, trace metals such as cobalt, nickel and zinc, can adsorb to the negatively charged surface of Mn oxides (Koschinsky and Hein, 2003). When

510 transport of Mn is in the form of dMn(III)-L instead of Mn oxides, these trace metals will no longer adsorb to the Mn oxides and the transport of the trace metals will be decoupled from the transport of Mn (Oldham et al., 2021; Lenstra et al., 2022).

Conclusions

515 Our combined seasonal field and modelling study reveals that dissolved Mn(III) (dMn(III)-L) is a key component of the Mn cycle in sediments of a seasonally euxinic coastal basin. Dissolved Mn(III) accounts for the majority of dissolved Mn in the pore water and coexists with high concentrations of H_2S. Results of a multicomponent reactive transport model indicate suggest that, at our study site, reduction of Mn oxides coupled to oxidation of Fe(II) and organic matter and oxidation of Mn(II) by O_2 are the primary sources of the dMn(III)-L when O_2 is present near the sediment water interface. However, when the bottom

520 waters are euxinic, reactions with dissolved Fe(II) likely dominate both the production and removal of dMn(III)-L. Modelled benthic Mn fluxes indicate suggest that while dMn(III)-L is released from the sediment throughout the year, there is a distinct seasonal contrast: in the model, release of dMn(III)-L dominates when bottom waters are oxic while a transition to euxinia leads to a temporary increased role for Mn(II). The benthic release of dMn(III)-L, both under oxic and euxinic bottom waters, in combination with a higher mobility of dMn(III)-L in the water column when compared to Mn(II), may contribute to lateral

525 transport of Mn from coastal zones to open marine waters.

Code and data availability

The data presented in this paper are available in the supplements. The data and model presented in the study are also deposited in the Zenodo repository, doi: 10.5281/zenodo.11475150. These will be made public upon acceptance of the paper.

Conflict of interest

530 The authors declare that they have no conflict of interest.

Acknowledgements

We thank the captain and crew of the R/V Navicula, A. Tramper and M. Hermans for their support during the sampling campaigns. We are also grateful to T. Claessen, C. Mulder, J. Visser and H. de Waard, for analytical assistance at Utrecht University. This research was financially supported by ERC Synergy grant MARIX (8540088) and the Netherlands Earth

535 System Science Center (NESSC 024002001). WKL acknowledges support from a NESSC Travel Grant and Veni grant VI.Veni.222.332 .

Author contributions

RK, WL and CS designed the research and wrote the paper with comments provided by all authors. OZ, NvH, and WL
540 performed the sampling. RK, OZ, NvH, and WL performed the geochemical analyses. VO instructed on the dissolved Mn(II)/Mn(III) method. RK and WL wrote the reactive transport model code and performed the model simulations. RK, OZ, NvH, WL, CS and MJ interpreted the data. All authors contributed to the article and approved the submitted version.

References

Aller, R. C.: The sedimentary Mn cycle in Long Island Sound: Its role as intermediate oxidant and the influence of bioturbation, O2, and Corg flux on diagenetic reaction balances. J. Mar. Res., 52(2), 259–295. https://doi.org/10.1357/0022240943077091, 1994.

Anschutz, P., Dedieu, K., Desmazes, F., & Chaillou, G.: Speciation, oxidation state, and reactivity of particulate manganese in marine sediments. Chem. Geol., 218(3–4), 265–279. https://doi.org/10.1016/j.chemgeo.2005.01.008, 2005.

APHA: Standard Methods for the Examination of Water and Wastewater. American Public Health Association–American Water Works Association–Water Environment Federation, 2005.

Beal, E. J., House, C. H., & Orphan, V. J.: Manganese- and iron-dependent marine methane oxidation. Science, 325(5937), 184–187. https://doi.org/10.1126/science.1169984, 2009.

Berelson, W., McManus, J., Coale, K., Johnson, K., Burdige, D., Kilgore, T., Colodner, D., Chavez, F., Kudela, R., & Boucher, J.: A time series of benthic flux measurements from Monterey Bay, CA. Cont. Shelf Res., 23(5), 457–481. https://doi.org/10.1016/S0278-4343(03)00009-8, 2003.

Boudreau, B. P.: The diffusive tortuosity of fine-grained unlithified sediments. Geochim. Cosmochim. Ac., 60(16), 3139–3142, 1996.

Breitburg, D., Levin, L. A., Oschlies, A., Grégoire, M., Chavez, F. P., Conley, D. J., Garçon, V., Gilbert, D., Gutiérrez, D., Isensee, K., Jacinto, G. S., Limburg, K. E., Montes, I., Naqvi, S. W. A., Pitcher, G. C., Rabalais, N. N., Roman, M. R., Rose, K. A., Seibel, B. A., … Zhang, J.: Declining oxygen in the global ocean and coastal waters. Science, 359(6371). https://doi.org/10.1126/science.aam7240, 2018

Burdige, D. J.: The biogeochemistry of manganese and iron reduction in marine sediments. Earth-Sci. Rev., 35, 249–284., 1993.

Calvert, S. E., & Pedersen, T. F.: Sedimentary Geochemistry of Manganese: Implications for the Environment of Formation of Manganiferous Black Shales. Econ. Geol., 91(3), 36–47, 1996.

Claff, S. R., Sullivan, L. A., Burton, E. D., & Bush, R. T.: A sequential extraction procedure for acid sulfate soils: Partitioning of iron. Geoderma, 155(3–4), 224–230. https://doi.org/10.1016/j.geoderma.2009.12.002, 2010.

Cline, J. D.: Spectrophotometric Determination of Hydrogen Sulfide in Natural Waters. Limnol. Oceanogr., 14(3), 454–458. https://doi.org/10.4319/lo.1969.14.3.0454

Dellwig, O., Schnetger, B., Meyer, D., Pollehne, F., Häusler, K., & Arz, H. W.: Impact of the major Baltic inflow in 2014 on manganese cycling in the gotland deep (Baltic Sea). Front. Mar. Sci., 5(JUL), 1–20. https://doi.org/10.3389/fmars.2018.00248, 2018.

Diaz, R. J., & Rosenberg, R.: Spreading dead zones and consequences for marine ecosystems. Science, 321(5891), 926–929. https://doi.org/10.1126/science.1156401, 2008.

Egger, M., Hagens, M., Sapart, C. J., Dijkstra, N., van Helmond, N. A. G. M., Mogollón, J. M., Risgaard-Petersen, N., van der Veen, C., Kasten, S., Riedinger, N., Böttcher, M. E., Röckmann, T., Jørgensen, B. B., & Slomp, C. P.: Iron oxide reduction in methane-rich deep Baltic Sea sediments. Geochim. Cosmochim. Ac.Geochim. Cosmochim. Ac., 207, 256–276. https://doi.org/10.1016/j.gca.2017.03.019, 2017.

Egger, M., Lenstra, W., Jong, D., Meysman, F. J. R., Sapart, C. J., Van Der Veen, C., Röckmann, T., Gonzalez, S., & Slomp,

C. P.: Rapid sediment accumulation results in high methane effluxes from coastal sediments. PLoS ONE, 11(8), 1–22. https://doi.org/10.1371/journal.pone.0161609, 2016.

Furukawa, K., & Takahashi, Y.: Effect of complexation with humic substances on diffusion of metal ions in water. Chemosphere, 73(8), 1272–1278. https://doi.org/10.1016/j.chemosphere.2008.07.017, 2008.

Grégoire, M., Garçon, V., Garcia, H., Breitburg, D., Isensee, K., Oschlies, A., Telszewski, M., Barth, A., Bittig, H. C., Carstensen, J., Carval, T., Chai, F., Chavez, F., Conley, D., Coppola, L., Crowe, S., Currie, K., Dai, M., Deflandre, B., … Yasuhara, M.: A Global Ocean Oxygen Database and Atlas for Assessing and Predicting Deoxygenation and Ocean Health in the Open and Coastal Ocean. Front. Mar. Sci., 8(December), 1–29. https://doi.org/10.3389/fmars.2021.724913, 2021.

Hermans, M., Pascual, M. A., Behrends, T., Lenstra, W. K., Conley, D. J., & Slomp, C. P.: Coupled dynamics of iron, manganese, and phosphorus in brackish coastal sediments populated by cable bacteria. Limnol. Oceanogr., 66, 2611–2631. https://doi.org/10.1002/lno.11776, 2021.

Hulth, S., Aller, R. C., & Gilbert, F.: Coupled anoxic nitrification / manganese reduction in marine sediments. Geochim. Cosmochim. Ac., 63(1), 49–66, 1999.

Jørgensen, B. B., Beulig, F., Egger, M., Petro, C., Scholze, C., & Røy, H.: Organoclastic sulfate reduction in the sulfate-methane transition of marine sediments. Geochim. Cosmochim. Ac., 254, 231–245. https://doi.org/10.1016/j.gca.2019.03.016, 2019.

Kalinichev, A. G., & Kirkpatrick, R. J.: Molecular dynamics simulation of cationic complexation with natural organic matter. Eur. J. Soil Sci., 58(4), 909–917. https://doi.org/10.1111/j.1365-2389.2007.00929.x, 2007.

Karolewski, J. S., Sutherland, K. M., Hansel, C. M., & Wankel, S. D.: ScienceDirect An isotopic study of abiotic nitrite oxidation by ligand-bound manganese (III). Geochim. Cosmochim. Ac., 293, 365–378. https://doi.org/10.1016/j.gca.2020.11.004, 2021.

Kim, B., Lingappa, U. F., Magyar, J., Monteverde, D., Valentine, J. S., Cho, J., & Fischer, W.: Challenges of measuring soluble Mn(III) species in natural samples. Molecules, 27(5), 1661, 2022.

Koschinsky, A., & Hein, J. R.. Uptake of elements from seawater by ferromanganese crusts: Solid-phase associations and seawater speciation. Mar. Geol., 198(3–4), 331–351. https://doi.org/10.1016/S0025-3227(03)00122-1, 2003.

Kostka, J. E., Luther, G. W., & Nealson, K. H.: Chemical and biological reduction of Mn (III)-pyrophosphate complexes: Potential importance of dissolved Mn (III) as an environmental oxidant. Geochim. Cosmochim. Ac., 59(5), 885–894. https://doi.org/10.1016/0016-7037(95)00007-0, 1995.

Kraal, P., Dijkstra, N., Behrends, T., & Slomp, C. P.: Phosphorus burial in sediments of the sulfidic deep Black Sea: Key roles for adsorption by calcium carbonate and apatite authigenesis. Geochim. Cosmochim. Ac., 204, 140-158, 2017.

Lenstra, W. K., Egger, M., Helmond, N. A. G. M. Van, Kritzberg, E., Conley, D. J. & Slomp, C.P.: Large variations in iron input to an oligotrophic Baltic Sea estuary : impact on sedimentary phosphorus burial. Biogeosciences, 6979–6996, 2018.

Lenstra, W. K., Hermans, M., Séguret, M. J. M., Witbaard, R., Severmann, S., Behrends, T., & Slomp, C. P.: Coastal hypoxia and eutrophication as key controls on benthic release and water column dynamics of iron and manganese. Limnol. Oceanogr., 66(3), 807–826. https://doi.org/10.1002/lno.11644, 2021.

Lenstra, W. K., Klomp, R., Molema, F., Behrends, T., & Slomp, C. P.: A sequential extraction procedure for particulate manganese and its application to coastal marine sediments. Chem. Geol., 584(June), 120538.

https://doi.org/10.1016/j.chemgeo.2021.120538, 2021.

Lenstra, W. K., Séguret, M. J. M., Behrends, T., Groeneveld, R. K., Hermans, M., Witbaard, R., & Slomp, C. P.: Controls on the shuttling of manganese over the northwestern Black Sea shelf and its fate in the euxinic deep basin. Geochim. Cosmochim. Ac., 273, 177–204. https://doi.org/10.1016/j.gca.2020.01.031, 2020.

Lenstra, W. K., van Helmond, N. A. G. M., Żygadłowska, O. M., van Zummeren, R., Witbaard, R., & Slomp, C. P.: Sediments as a Source of Iron, Manganese, Cobalt and Nickel to Continental Shelf Waters (Louisiana, Gulf of Mexico). Front. Mar. Sci., 9(January), 1–13. https://doi.org/10.3389/fmars.2022.811953, 2022.

Lenz, C., Jilbert, T., Conley, D. J., Wolthers, M., & Slomp, C. P.: Are recent changes in sediment manganese sequestration in the euxinic basins of the Baltic Sea linked to the expansion of hypoxia? Biogeosciences, 12(16), 4875–4894. https://doi.org/10.5194/bg-12-4875-2015, 2015.

Lepland, A., & Stevens, R. L.: Manganese authigenesis in the Landsort Deep, Baltic Sea. Mar. Geol., 151(1–4), 1–25. https://doi.org/10.1016/S0025-3227(98)00046-2, 1998.

Luther, G. W.: Manganese(II) oxidation and Mn(IV) reduction in the environment - Two one-electron transfer steps versus a single two-electron step. Geomicrobiol. J., 22(3–4), 195–203. https://doi.org/10.1080/01490450590946022, 2005.

Luther, G. W., Madison, A. S., Mucci, A., Sundby, B., & Oldham, V. E.: A kinetic approach to assess the strengths of ligands bound to soluble Mn(III). Mar. Chem., 173, 93–99. https://doi.org/10.1016/j.marchem.2014.09.006, 2015.

Luther III, G. W.: The role of one- and two-electron transfer reactions in forming thermodynamically unstable intermediates as barriers in multi-electron redox reactions. Aquat. Geochem. , 16(3), 395–420. https://doi.org/10.1007/s10498-009-9082-3, 2010.

Luther III, G. W., Thibault de Chanvalon, A., Oldham, V. E., Estes, E. R., Tebo, B. M., & Madison, A. S.: Reduction of Manganese Oxides : Thermodynamic , Kinetic and Mechanistic Considerations for One - Versus Two - Electron Transfer Steps. Aquat. Geochem. , 24, 257–277. https://doi.org/10.1007/s10498-018-9342-1, 2018.

Madison, A. S., Tebo, B. M., & Luther, G. W.: Simultaneous determination of soluble manganese(III), manganese(II) and total manganese in natural (pore)waters. Talanta, 84(2), 374–381. https://doi.org/10.1016/j.talanta.2011.01.025, 2011

Madison, A. S., Tebo, B. M., Mucci, A., Sundby, B., & Luther III, G. W.: Abundant Porewater Mn(III) Is a Major Component of the Sedimentary Redox System. Science, 341(August), 875–878. https://doi.org/10.5040/9780755621101.0007, 2013.

McManus, J., Berelson, W. M., Severmann, S., Johnson, K. S., Hammond, D. E., Roy, M., & Coale, K. H.: Benthic manganese fluxes along the Oregon-California continental shelf and slope. Cont. Shelf Res., 43, 71–85. https://doi.org/10.1016/j.csr.2012.04.016, 2012.

Neretin, L. N., Pohl, C., Leipe, T., & Pollehne, F.: Manganese cycling in the Gotland Deep , Baltic Sea. Mar. Chem., 82, 125–143, 2003.

Oldham, V. E., Chmiel, R., Hansel, C. M., DiTullio, G. R., Rao, D., & Saito, M.: Inhibited Manganese Oxide Formation Hinders Cobalt Scavenging in the Ross Sea. Global Biogeochem. Cy., 35(5), 1–14. https://doi.org/10.1029/2020GB006706, 2021.

Oldham, V. E., Miller, M. T., Jensen, L. T., & Luther, G. W.: Revisiting Mn and Fe removal in humic rich estuaries. Geochim. Cosmochim. Ac., 209, 267–283. https://doi.org/10.1016/j.gca.2017.04.001, 2017.

Oldham, V. E., Mucci, A., Tebo, B. M., & Luther, G. W.: Soluble Mn(III)–L complexes are abundant in oxygenated waters

and stabilized by humic ligands. Geochim. Cosmochim. Ac., 199, 238–246. https://doi.org/10.1016/j.gca.2016.11.043, 2017.

Oldham, V. E., Owings, S. M., Jones, M. R., Tebo, B. M., & Luther, G. W.: Evidence for the presence of strong Mn(III)-binding ligands in the water column of the Chesapeake Bay. Mar. Chem., 171, 58–66. https://doi.org/10.1016/j.marchem.2015.02.008, 2015.

Oldham, V. E., Siebecker, M. G., Jones, M. R., Mucci, A., Tebo, B. M., & Luther, G. W.: The Speciation and Mobility of Mn and Fe in Estuarine Sediments. Aquat. Geochem. , 25(1–2), 3–26. https://doi.org/10.1007/s10498-019-09351-0, 2019.

Pakhomova, S. V., Hall, P. O. J., Kononets, M. Y., Rozanov, A. G., Tengberg, A., & Vershinin, A. V.: Fluxes of iron and manganese across the sediment-water interface under various redox conditions. Mar. Chem., 107(3), 319–331. https://doi.org/10.1016/j.marchem.2007.06.001, 2007.

Poulton S. W. and Canfield D. E.: Development of a sequential extraction procedure for iron: implications for iron partitioning in continentally derived particulates. Chem. Geol. 214, 209–221, 2005.

Postma, D.: Concentration of Mn and separation from Fe in sediments-I . Kinetics and stoichiometry of the reaction between biiessite and dissolved Fe (H) at 10 ° C. Geochim. Cosmochim. Ac., 49, 1023–1033, 1985.

Raiswell, R., & Canfield, D. E.: The Iron Biogeochemical Cycle Past and Present. Geochem. Perspect., 1, 2012.

Raven, J. A.: Predictions of Mn and Fe use efficiencies of phototrophic growth as a function of light availability for growth and of C assimilation pathway. New Phytol., 116(1), 1–18. https://doi.org/10.1111/j.1469-8137.1990.tb00505.x, 1990.

Reed, D. C., Slomp, C. P., & Gustafsson, B. G.: Sedimentary phosphorus dynamics and the evolution of bottom-water hypoxia: A coupled benthic-pelagic model of a coastal system. Limnol. Oceanogr., 56(3), 1075–1092. https://doi.org/10.4319/lo.2011.56.3.1075, 2011.

Sander, S. G., & Koschinsky, A.: Metal flux from hydrothermal vents increased by organic complexation. Nat. Geosci, 4(3), 145–150. https://doi.org/10.1038/ngeo1088, 2011.

Slomp, C. P., Malschaert, J. F. P., Lohse, L., & Van Raaphorst, W.: Iron and manganese cycling in different sedimentary environments on the North Sea continental margin. Science, 17(9), 1083–1117, 1997.

Soetaert, K., & Meysman, F.: Environmental Modelling & Software Reactive transport in aquatic ecosystems : Rapid model prototyping in the open source software R. Environ Model Softw, 32, 49–60. https://doi.org/10.1016/j.envsoft.2011.08.011, 2012.

Soetaert, K., Petzoldt, T., & Meysman, F.: marelac : Tools for Aquatic Sciences, 2010.

Solórzano, L.: Determination of Ammonia in Natural Waters by the Phenolhypochlorite Method. Limnol. Oceanogr., 14(September), 799–801. https://doi.org/10.4319/ lo.1969.14.5.0799, 1968.

Sulu-Gambari, F., Roepert, A., Jilbert, T., Hagens, M., Meysman, F. J. R., & Slomp, C. P.: Molybdenum dynamics in sediments of a seasonally-hypoxic coastal marine basin. Chem. Geol., 466(April), 627–640. https://doi.org/10.1016/j.chemgeo.2017.07.015, 2017.

Thamdrup, B., & Dalsgaard, T.: The fate of ammonium in anoxic manganese oxide-rich marine sediment. Geochim. Cosmochim. Ac., 64(24), 4157–4164., 2000.

Thibault de Chanvalon, A., & Luther, G. W.: Mn speciation at nanomolar concentrations with a porphyrin competitive ligand

and UV–vis measurements. Talanta, 200, 15-21, 2019.

Trouwborst, R. E., Clement, B. G., Tebo, B. M., Glazer, B. T., & Luther, G. W.: Soluble Mn(III) in suboxic zones. Science, 313(5795), 1955–1957. https://doi.org/10.1126/science.1132876, 2006.

Van Cappellen, P., & Wang, Y.: Cycling of iron and manganese in surface sediments: a general theory for the coupled transport and reaction of carbon, oxygen, nitrogen, sulfur, iron and manganese. Am. J. Sci., 296(March), 197–243, 1996.

van der Zee, C., van Raaphorst, W., & Epping, E.: Absorbed Mn2+ and Mn redox cycling in Iberian continental margin sediments (northeast Atlantic Ocean). J. Mar. Res., 59, 133–166, 2001.

Van Santvoort, P. J. M., De Lange, G. J., Thomson, J., Colley, S., Meysman, F. J. R., & Slomp, C. P.: Oxidation and origin of organic matter in surficial Eastern Mediterranean hemipelagic sediments. Aquat. Geochem. , 8(3), 153–175. https://doi.org/10.1023/A:1024271706896, 2002.

Yakushev, E. V., Pollehne, F., Jost, G., Kuznetsov, I., Schneider, B., & Umlauf, L.: Analysis of the water column oxic/anoxic interface in the Black and Baltic seas with a numerical model. Mar. Chem., 107(3), 388–410. https://doi.org/10.1016/j.marchem.2007.06.003, 2007.

Żygadłowska, O. M., Venetz, J., Klomp, R., Lenstra, W. K., Van Helmond, N. A. G. M., Röckmann, T., Wallenius, A. J., Dalcin Martins, P., Veraart, A. J., Jetten, M. S. M., & Slomp, C. P.: Pathways of methane removal in the sediment and water column of a seasonally anoxic eutrophic marine basin. Front. Mar. Sci., January, 1–15. https://doi.org/10.3389/fmars.2023.1085728, 2023.

Zygadłowska, O. M., van Helmond, N. A. G. M., Lenstra, W. K., Klomp, R., Accou, R., Puyk, R., Dickson, A. J., Jetten, M. S. M., & Slomp, C. P.: Seasonal euxinia in a coastal basin: Impact on sedimentary molybdenum enrichments and isotope signatures. Chem. Geol., 670(September), 122297. https://doi.org/10.1016/j.chemgeo.2024.122297, 2024a.

Żygadłowska, O. M., Venetz, J., Lenstra, W. K., Van Helmond, N. A. G. M., Klomp, R., Röckmann, T., & Slomp, C. P.: Ebullition drives high methane emissions from a eutrophic coastal basin. Geochim. Cosmochim. Ac., 384, 1–13. https://doi.org/10.1016/j.gca.2024.08.028, 2024b.

Supplements to: Dissolved Mn(III) is a key redox intermediate in sediments of a seasonally euxinic coastal basin

1.   Description of the fieldwork campaigns performed in 2021

Sampling of the sediment at Scharendijke basin was performed during 8 sampling campaigns with RV *Navicula* each month
5   from March to October 2021, following the same methods used in the fieldwork campaigns in 2020 presented in this study.
An additional sampling event in August / September 2021 is reported in Żygadłowska et al. (2024a, b). These results are not
included here, because we focus on the monthly output of the reactive transport model. During each campaign, a sediment
core was collected using a UWITEC corer with a transparent PVC core liner (120 cm length, 6 cm inner diameter) to collect
samples for NH_4^+, alkalinity, SO_4^{2-}, H_2S, TD Fe, TD Mn and during four campaigns, for the determination of Mn oxide and
10 Mn carbonate. The core was sectioned at a 1 cm resolution under a N_2 environment, the sections were subsequently centrifuged
to separate the pore water from the solid phase. The supernatant was filtered over 0.45 µm pore size filters. Samples for the
analysis of NH_4^+ were stored at -20°C and later analyzed using the indophenol blue method (Solórzano, 1968). The samples
for alkalinity and SO_4^{2-} were stored at 4°C until analysis. Alkalinity was measured through titration with 0.01 M HCl, within
24 h after sampling and SO_4^{2-} was measured using ion chromatography (Metrohm 930 Compact IC Flex; detection limit for
15 SO_4^{2-} of 50 µmol L^{-1}). The samples for H_2S analysis were diluted five times in a 2% Zn-acetate solution in a glass vial and
stored at 4°C. These samples were analyzed using the phenylenediamine and ferric chloride method (Cline, 1969). Samples
for TD Fe and Mn were acidified with 10 µL 35% suprapure HCl per ml of sample and stored at 4°C. These samples were
analyzed via ICP-OES (Perkin Elmer Avio; detection limit 0.1 µmol L^{-1} and 0.03 µmol L^{-1} for Fe and Mn respectively).
Samples for the analysis of the sediment residues were stored in N_2 purged aluminum bags at -20°C. Later, the samples were
20 freeze-dried and ground with an agate mortar and pestle under a N_2 environment. Solid phase speciation of Mn was then
determined using a sequential extraction procedure as described in Lenstra et al. (2021).

1.2.   Detailed model description

25 The reactions in the model describe organic matter (OM) degradation involving a range of electron acceptors combined with
secondary reactions of the reaction products (Table S5). Degradation of OM is facilitated, in successive order, by reduction of
O_2, NO_3^-, MnO_2, $Fe(OH)_3$ and SO_4^{2-} and finally OM is degraded via methanogenesis (Table S2; Froelich et al., 1979; Reed et
al., 2011; Rooze et al., 2016). Monod kinetics are used to describe the sequence of electron acceptors in OM degradation
(Boudreau, 1997). In Monod kinetics, the oxidant with the highest metabolic free energy yield is used preferentially, until this
30 species becomes limiting and the next oxidant in the sequence is used preferentially (Boudreau, 1996; Van Cappellen & Wang,

1996). The OM is assumed to include carbon (C), nitrogen (N) and phosphorus (P) in a ratio of C:N:P = 106:15.45:1 (based on Egger et al., 2016b). Hence, the rate of OM degradation in the sediment is directly linked to the NH_4^+ profiles. In the model, reduction of MnO_2 can be coupled to oxidation of OM, Fe(II), H_2S and CH_4 (Table S2). Reduction of MnO_2 by OM, Fe(II) and H_2S is modelled as one electron transfer steps with Mn(III) as the product (Madison et al., 2013). Reduction of MnO_2 by CH_4 is modelled as a two electron transfer with Mn(II) as a product, because, to our knowledge, the one electron transfer step that is theoretically possible has never been demonstrated. Reduction of MnO_2 with NH_4^+ as discussed by (Hulth et al., 1999) and (Thamdrup and Dalsgaard, 2000) is not incorporated in the model, because the quantitative importance of this reaction is not well known. Reduction of dMn(III)-L is assumed to occur with Fe(II), H_2S and OM to form Mn(II), while oxidation of Mn(III) is assumed to occur with O_2 to form MnO_2. Reduction of dMn(III)-L by NO_2^- as described by Karolewski et al. (2021) is not incorporated in the model. Production of NO_2^- in the anoxic sediment is unlikely and concentrations in September are below the detection limit. Oxidation of Mn(II) with O_2 and precipitation as $MnCO_3$ removes Mn(II). Dissolved inorganic carbon in the model is the sum of carbon in HCO_3^{2-} and CO_2, which are produced or consumed in reactions. The dominant effect of adsorption of dissolved Mn(II) to solid phase Mn is related to transport through bioturbation (Slomp et al., 1997). At sites with little or no bioturbation, as is the case here, the effect of Mn(II) adsorption on modelled pore water profiles will be limited.

Depending on whether a compound is a solid or solute, its generic mass conservation is described by Eq. 1 or Eq. 2, respectively.

$$(1 - \varphi) \frac{\partial C_s}{\partial t} = -(1 - \varphi)v \frac{\partial C_s}{\partial z} + \sum R_s \tag{1}$$

$$\varphi \frac{\partial C_{aq}}{\partial t} = \varphi D' \frac{\partial^2 C_{aq}}{\partial z^2} - \varphi u \frac{\partial C_{aq}}{\partial z} + \sum R_{aq} \tag{2}$$

In these equations, φ is the sediment porosity, t is time (yr), C_s and C_{aq} are the concentrations of the solid and dissolved species (mol L^{-1}), respectively, D' is the diffusion coefficient of dissolved species in the porous medium (cm^2 yr^{-1}), z is the distance from the Sediment-Water Interface (SWI; cm), v and u (cm yr^{-1}) are advective velocities of solids and dissolved species, respectively and $\sum R_s$ and $\sum R_{aq}$ are net rates of chemical reactions of solid and dissolved species, respectively.

For porosity, a depth-dependent function is used to account for sediment compaction (Meysman et al., 2005; Reed 2011a) (eq 3):

$$\varphi(z*) = \varphi_\infty + (\varphi_0 - \varphi_\infty)e^{-\frac{y}{z*}} \tag{3}$$

In this equation, φ_0 is the porosity at the SWI, φ_∞ is the porosity at depth and y is the porosity attenuation factor/e-folding distance (Table 3S5).

In the last 20 years of the model run, the seasonal cycle of oxic – euxinic conditions was simulated by varying the bottom water O_2 and H_2S concentration, the influx of Fe oxides, Mn oxides, Mn carbonates and OM and the sedimentation rate (Fig. S~~1~~3). The boundary conditions for the bottom water concentration of O_2 were based on monitoring by Rijkswaterstaat

60 (Directorate-General for Public Works and Water Management of the Netherlands) as reported in Żygadłowska et al. (2023a). The bottom water H_2S was varied together with O_2 and was either 0, or the concentration measured in the bottom water in September (111.8 μmol L^{-1}~~M~~). Input of metal oxides was varied together with O_2 and was fitted to the sediment profiles. The input of Mn carbonates was also varied to fit the sediment profiles, because authigenic Mn carbonate formation alone was insufficient to induce the observed oscillations. OM input was varied to fit the sediment profiles. The input of OM and the

65 sedimentation rate in April differ from those in the other oxic months, because the effect of a spring bloom ~~is~~was simulated. Such variations in OM input are in line with variations in primary productivity and OM supply from the North Sea known for this system (Hagens et al., 2015). Sedimentation rates for the model run until 201~~4~~6 (~~6~~4 years before the end of the model run) were based on Egger et al. (2016; 13.3 cm yr^{-1}). Between 60 – 80 cm depth, which is around where the shift in sedimentation rates is assumed, a shift in the oscillations is visible in for example the C_{org} and Mn oxides sediment profiles

70 (Fig. 4). This shift is modelled by varying the input of these compounds through the seasons. For the last ~~6~~4 years the sedimentation rate was set to 20 cm yr^{-1}, based on the onset of the shallowest peak in C_{org} at 20 cm depth (Fig. 4), which marks the C_{org} deposition of the previous year (i.e. spring 2019).
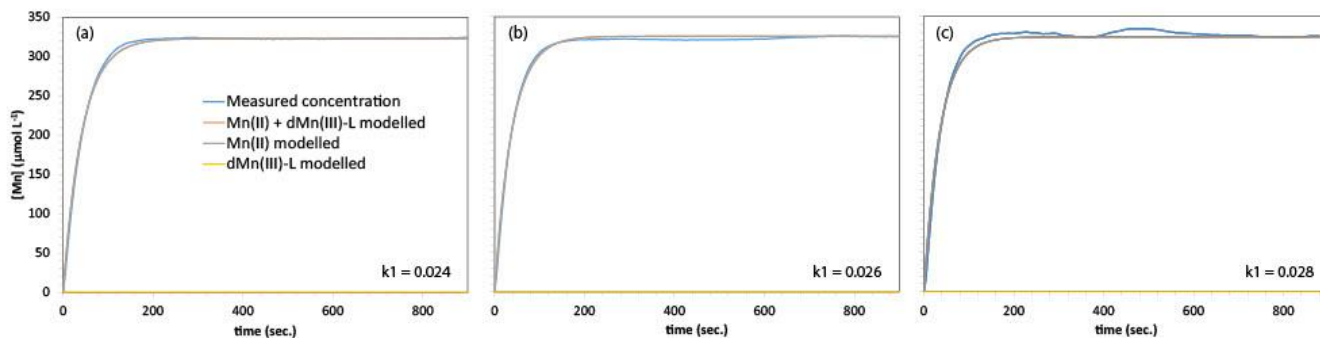
2.3. Figures

Figure S1: Kinetic curves (triplicates) that were used to determine the k1 value for the kinetic reaction of Mn(II) at this site. In the lower right corner of the graph, the k1 values are indicated.
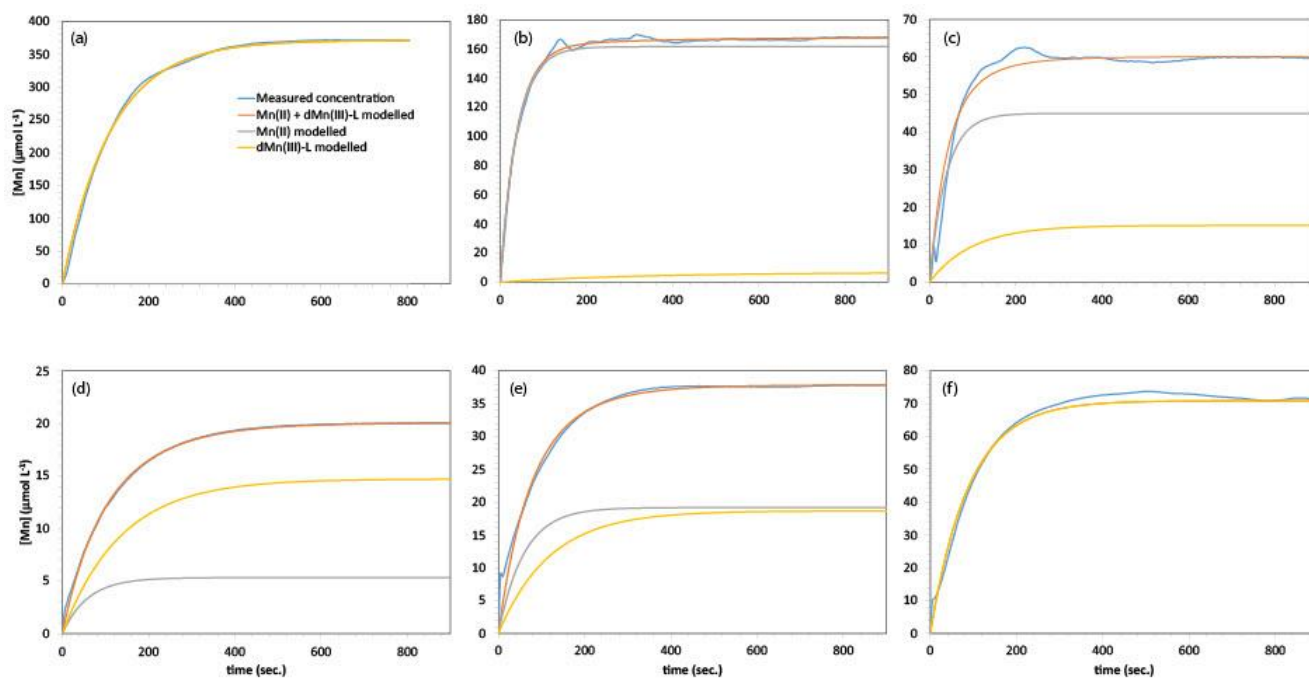
Figure S2, Kinetic curves that were measured and modelled Mn(II) and dMn(III)-L concentrations used to determine the Mn(II) and dMn(III)-L content of the samples from (a) 0 – 1 cm; (b) 6 – 7 cm; (c) 43 – 44 cm; in March 2020 and (d) 1 – 2 cm; (e) 7 – 8 cm; (f) 23 – 24 cm in September 2020.
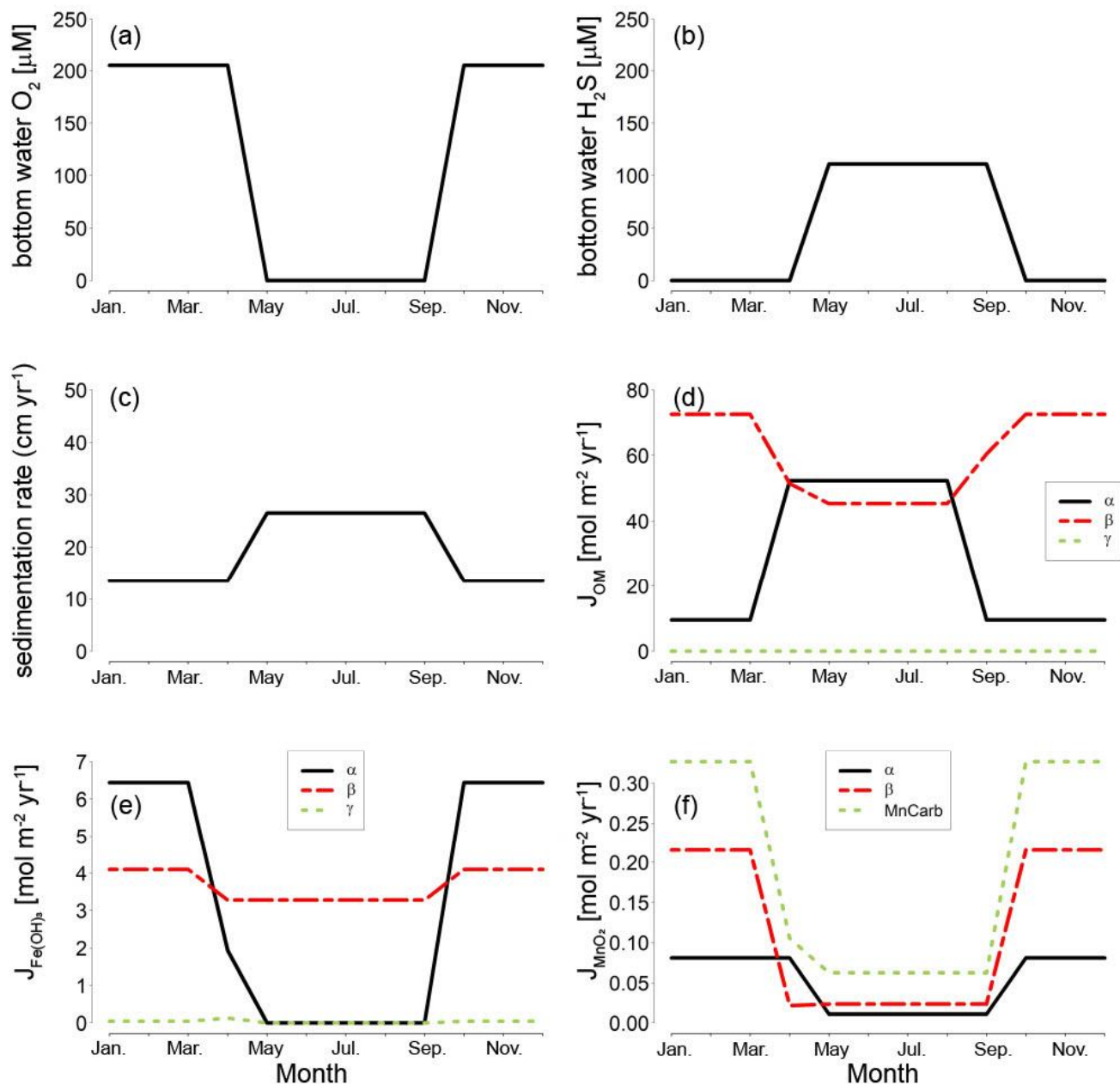
Figure S3~~1~~. Seasonal variation in bottom water O₂ and H₂S, sedimentation rate, and in the flux of Fe oxides ($J_{Fe(OH)_3}$), flux of Mn oxides ((J_{MnO_2}) and flux of organic matter (J_{OM}) at the sediment-water interface in the final year of the model simulations.
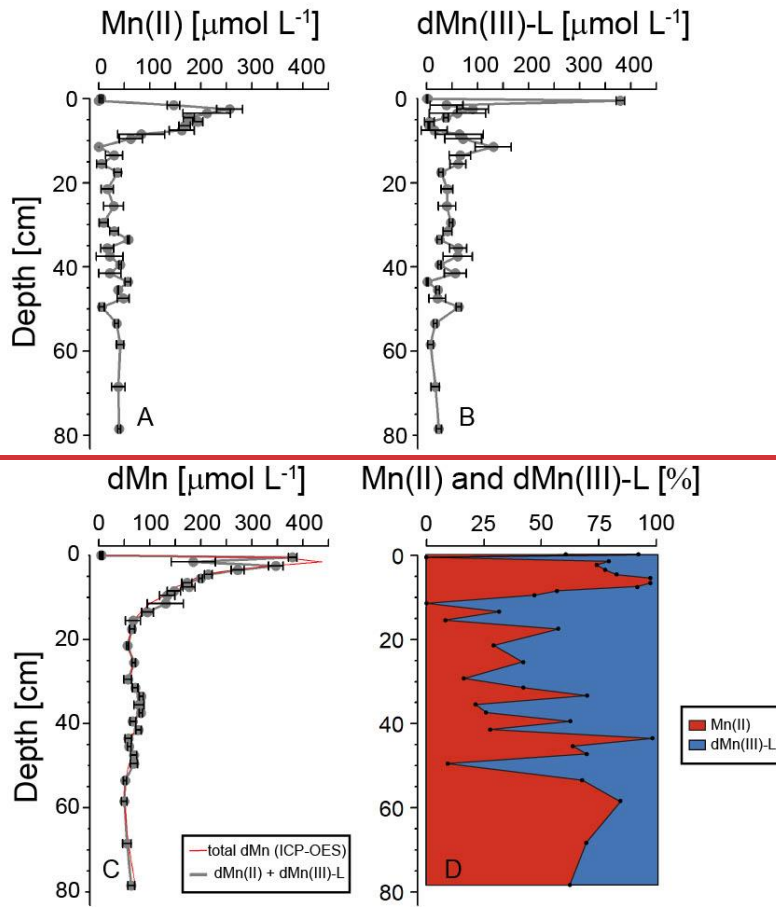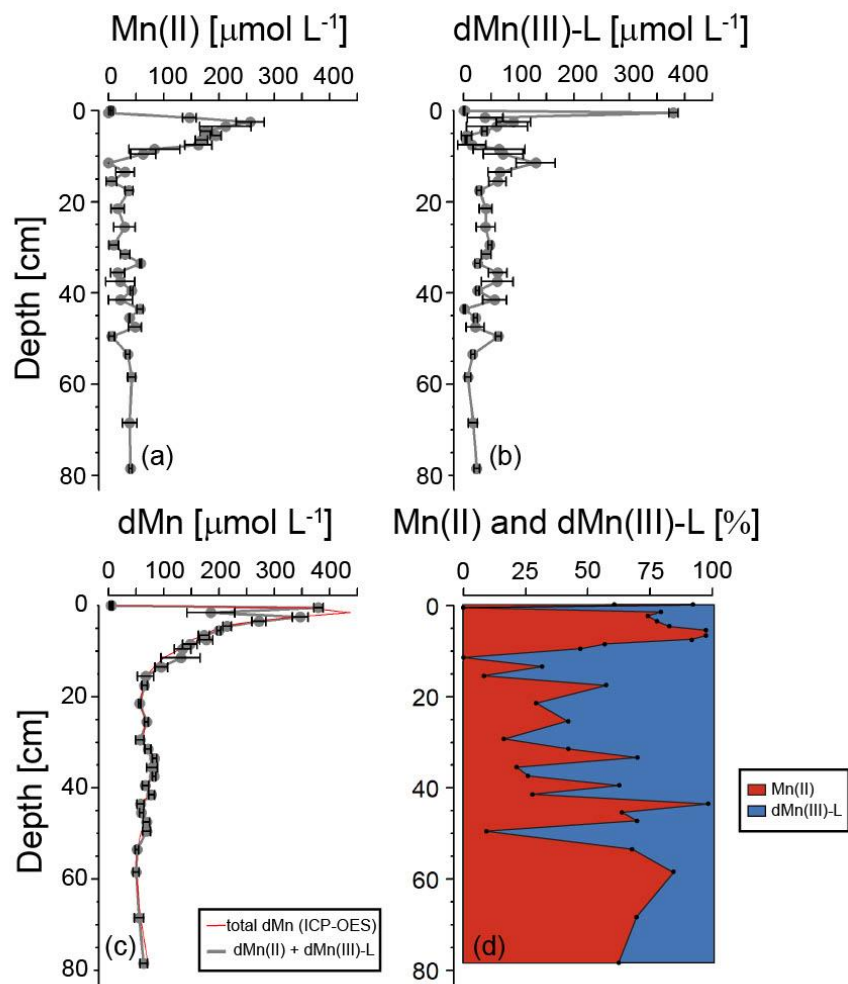
Figure S4: (a), (b) Data collected through spectrophotometric analysis of Mn(II) and dMn(III)-L in March, including error bars showing standard deviation (n=3). (c) The sum of Mn(II) and dMn(III)-L measured spectrophotometrically, including error bars showing standard deviation (n=3), compared with the total dissolved Mn measured with ICP-OES. (d) The contribution of Mn(II) and dMn(III)-L to the total dissolved Mn pool (determined as the sum of Mn(II) and dMn(III)-L) as percentage.
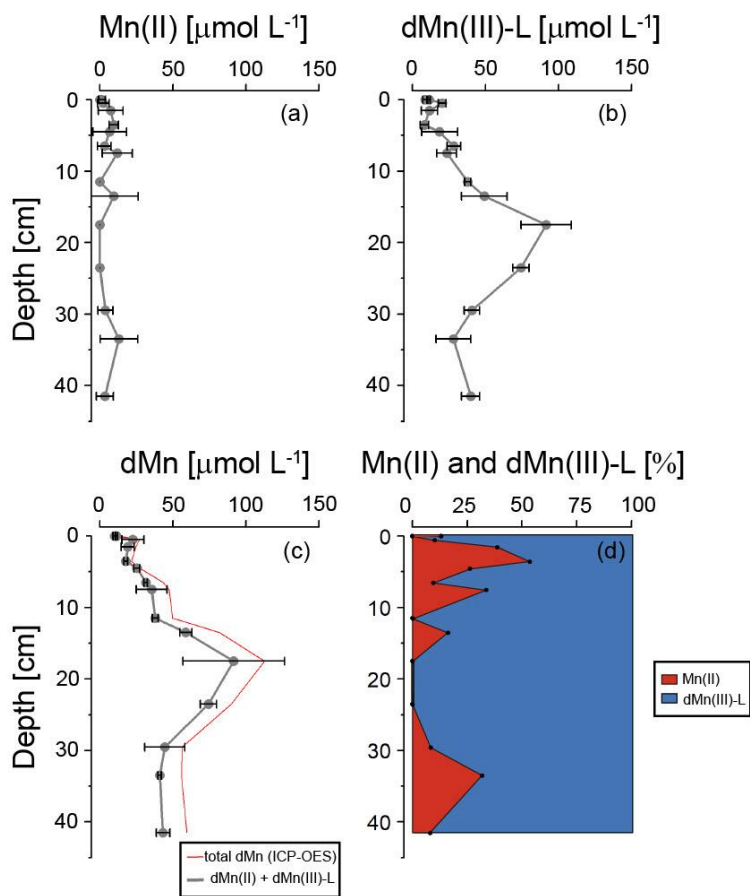
Figure S5̶3̶: (a)A̶, B̶)(b) Data collected during the spectrophotometric analysis of Mn(II) and dMn(III)-L in September, including error bars showing standard deviation (n = 3). C̶)(c) The sum of Mn(II) and dMn(III)-L measured during the spectrophotometric method including error bars (n = 3), compared with the total dissolved Mn measured with ICP-OES. D̶)(d) The contribution of Mn(II) and dMn(III)-L to the total dissolved Mn pool (determined as the sum of Mn(II) and dMn(III)-L) as a percentage.
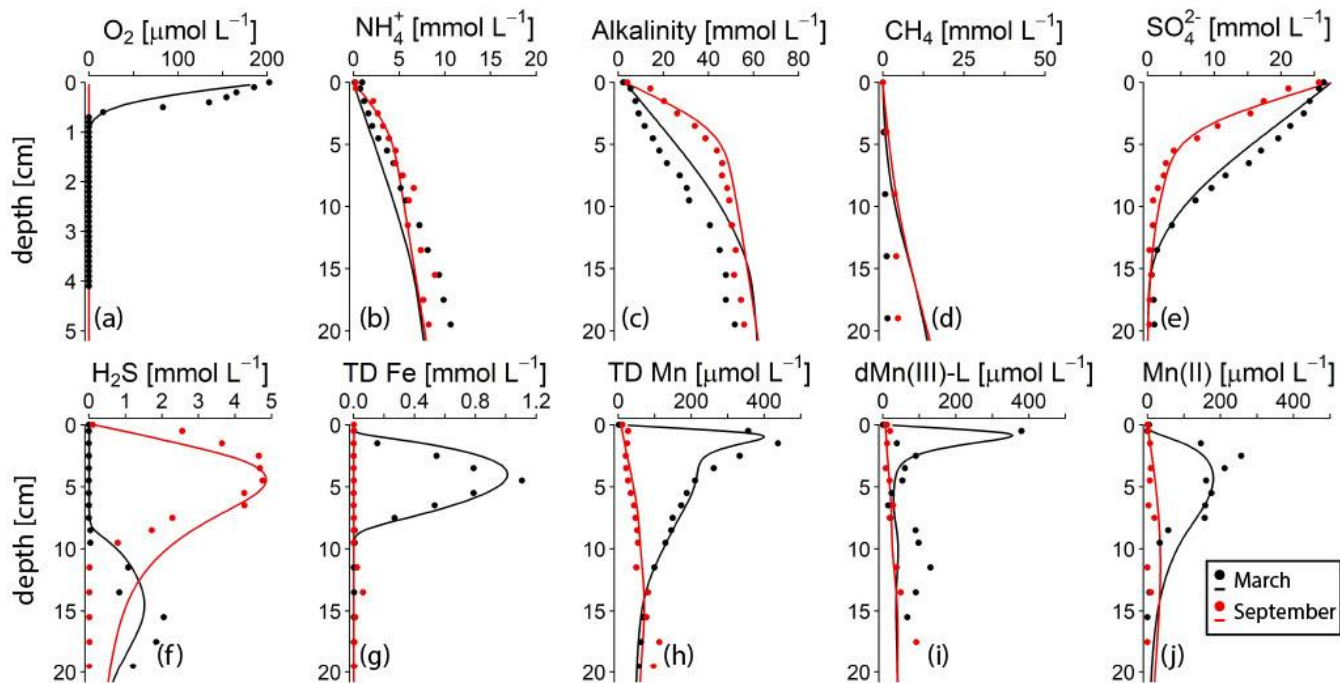
Figure S6. Top 20 cm of the pore water profiles of key components in March (black) and September (red) 2020. The dots represent measured concentrations, the lines indicate the results of the reactive transport model. Note the different depth scale on the y-axis for O_2. TD Fe and TD Mn refer to total dissolved Fe and total dissolved Mn. Profiles of Mn(II) and dMn(III)-L with standard deviation error bars (n =3) and the contribution to TD Mn (in %) can be found in Fig. S2, S3. No O_2 was detected in the sediment in September 2020 (Żygadłowska et al. 2023).
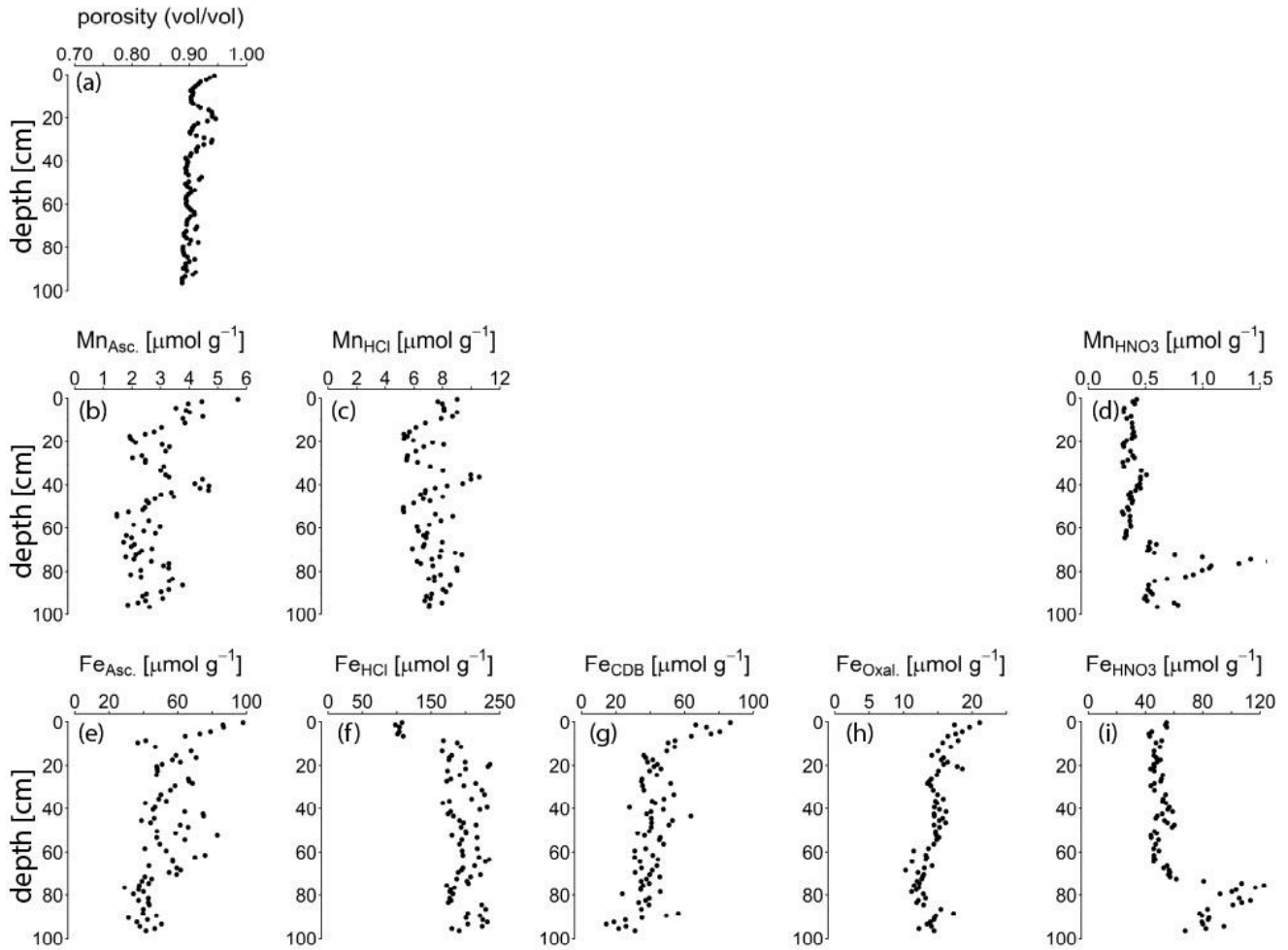
110

Figure S47: Porosity and all Mn and Fe fractions as determined in the sequential extraction, for the sediment collected in March 2020.
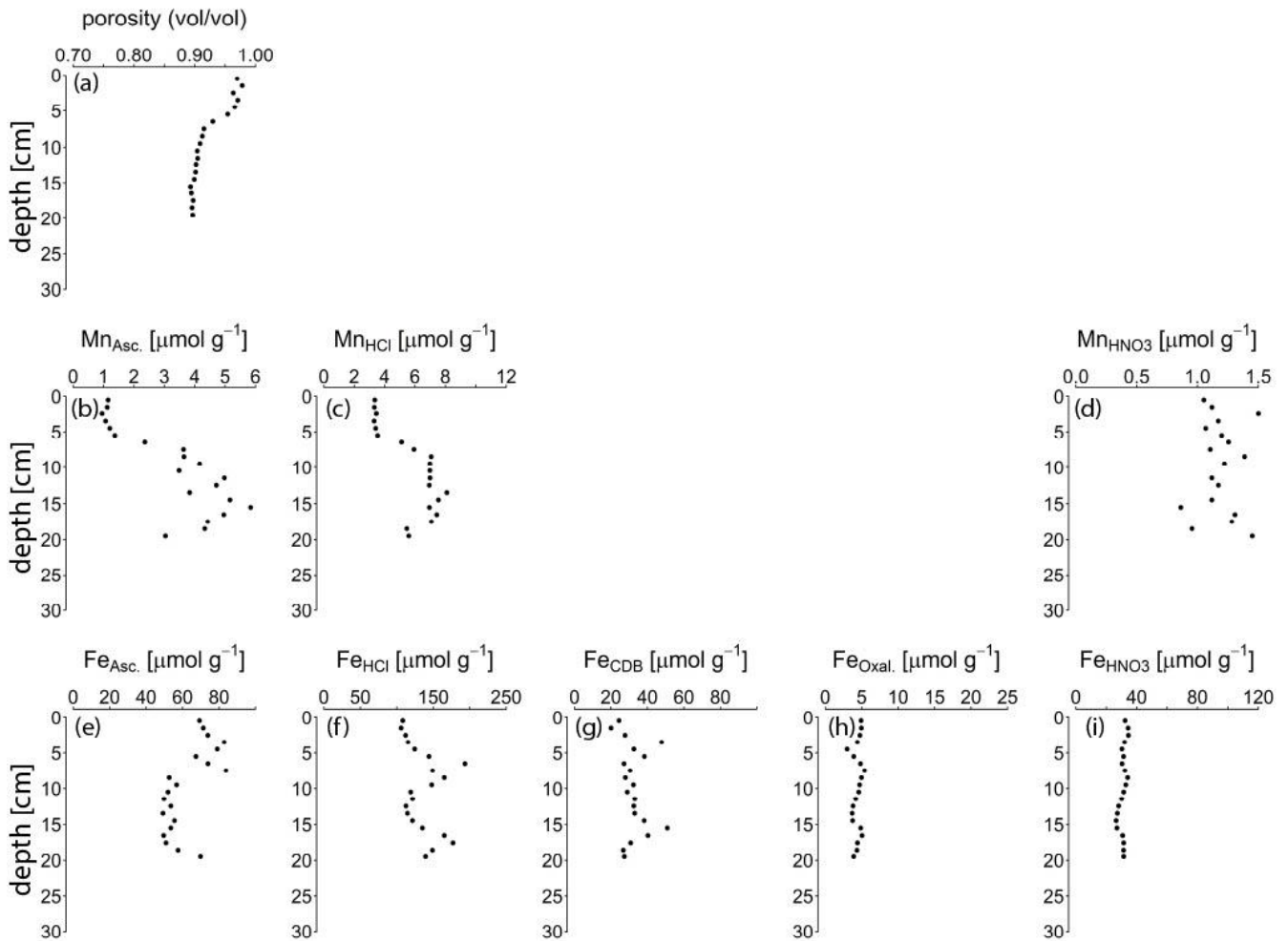
Figure S85: Porosity and all fractions extracted for Mn and Fe in the sequential extraction, for the sediment collected in September 2020 (0-20 cm).
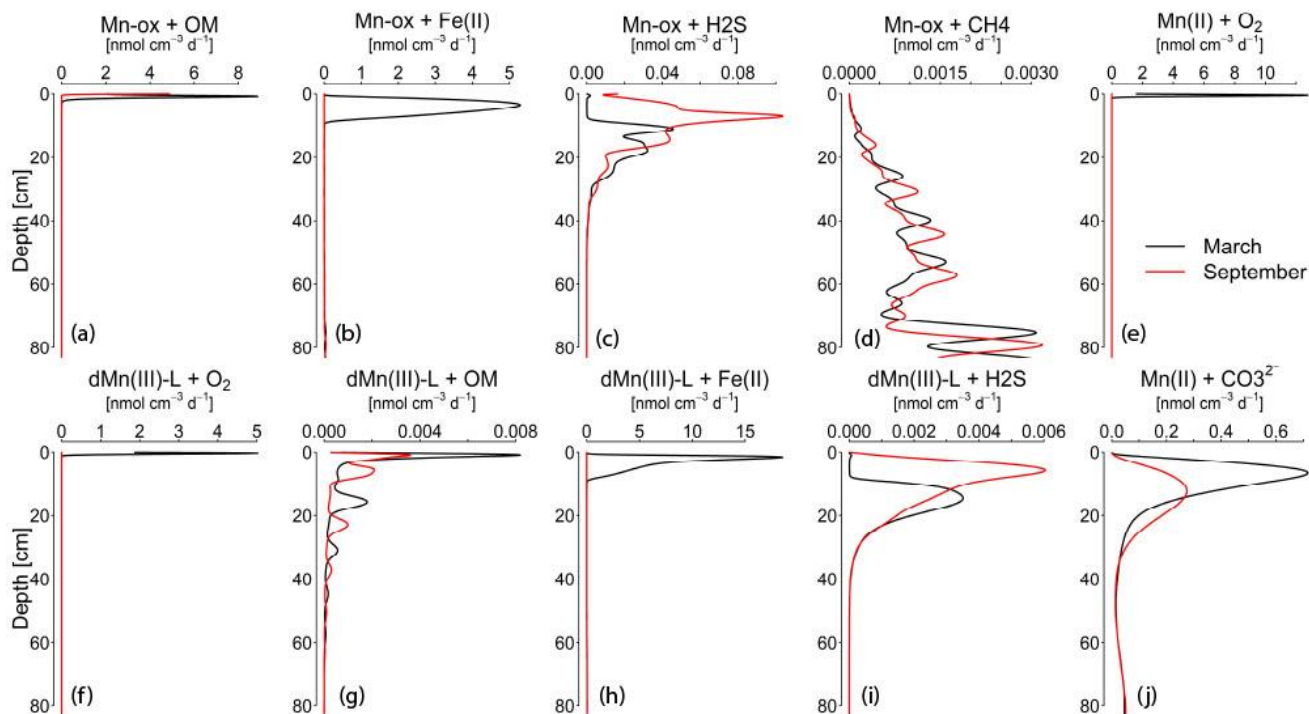
Figure S96: Depth profiles of the reaction rates, which form the basis for the rate integrations shown in Fig. 4.

120
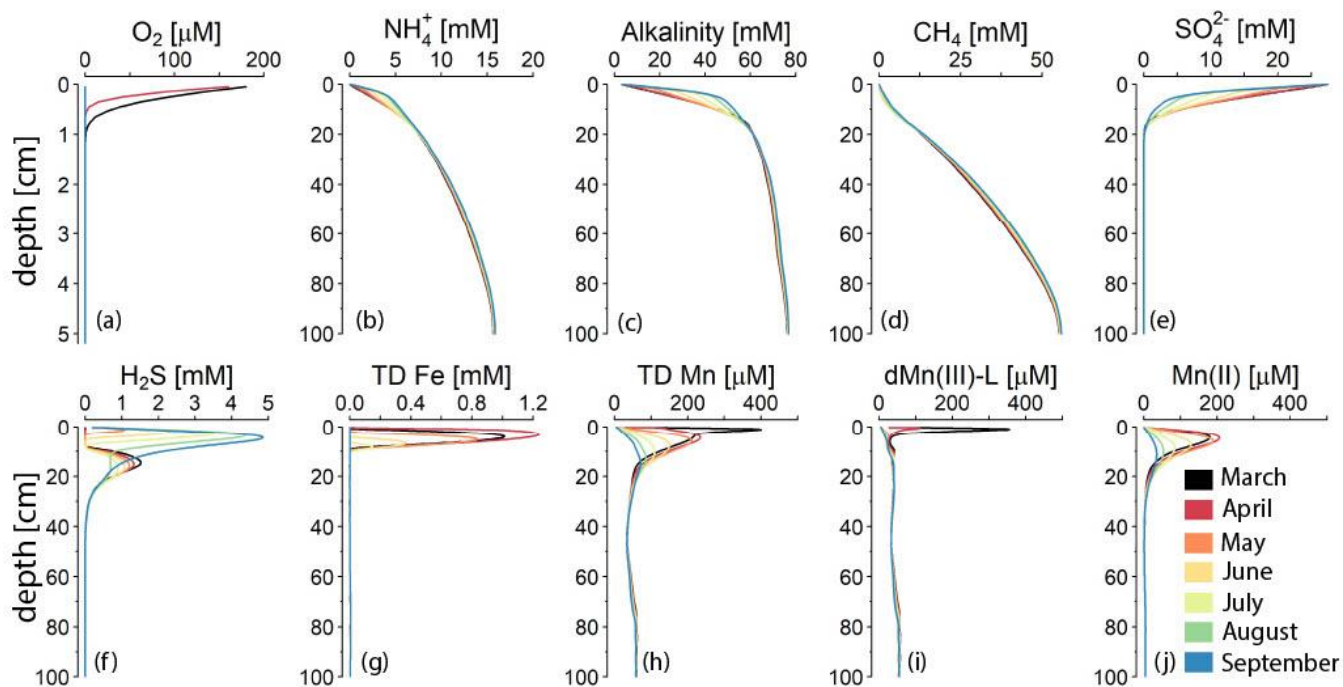
Figure S10~~7~~. The change in pore water profiles between March and September when anoxic conditions develop in the basin. With the reactive transport model, pore water profiles can be extrapolated to months where no fieldwork was done in 2020.
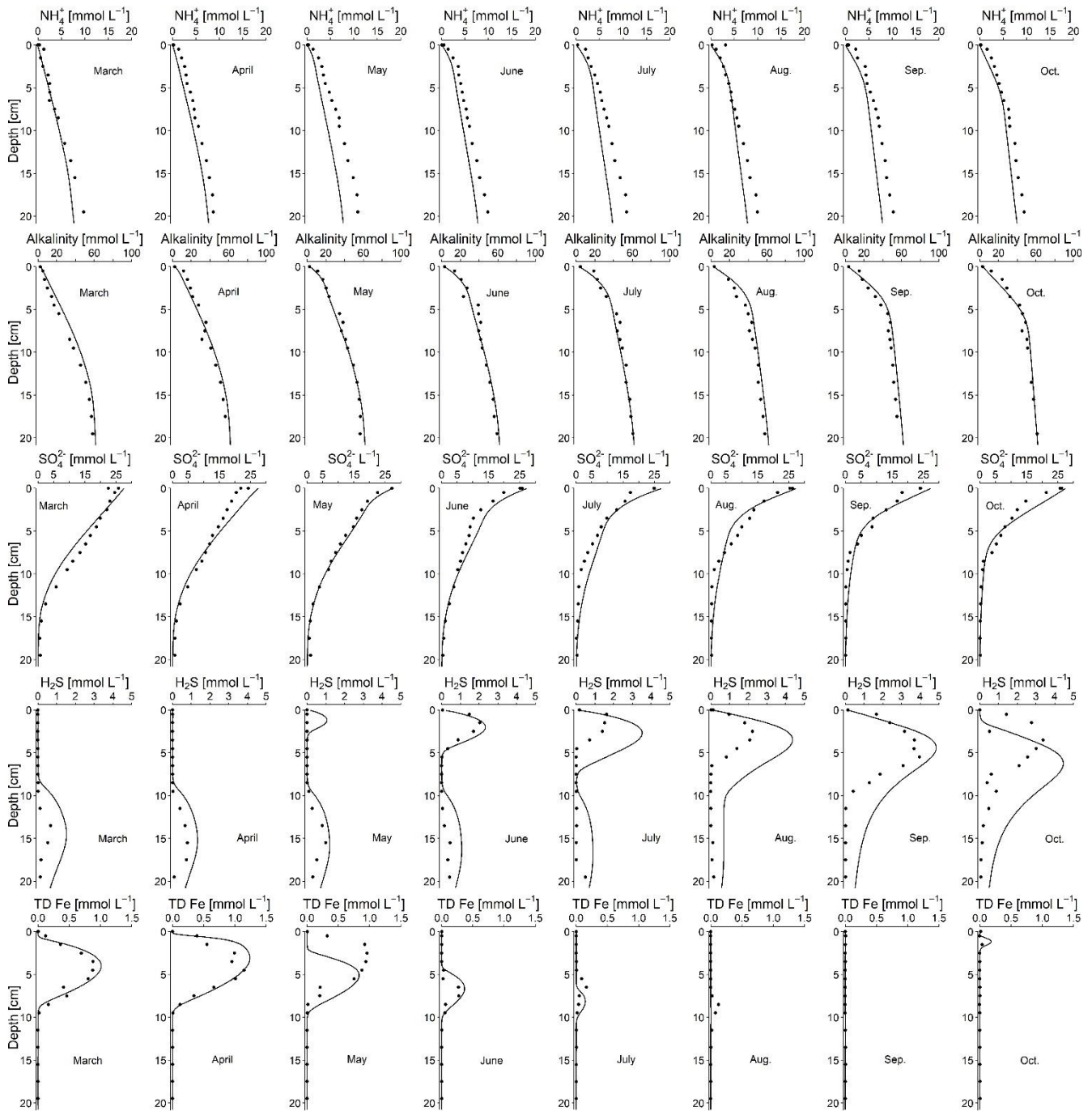
125 **Figure S11: Forward simulation of the reactive transport model to NH₄⁺, alkalinity, SO₄²⁻, H₂S, TD Fe, TD Mn and, for 4 months, Mn oxides and Mn carbonates obtained during 8 sampling campaigns performed between March and October 2021. In 2021, Scharendijke experienced euxinia from June until September (Żygadłowska et al., 2024a). Part of this dataset was previously published in Żygadłowska et al. (2024a, b). The figure continues on the next page.**
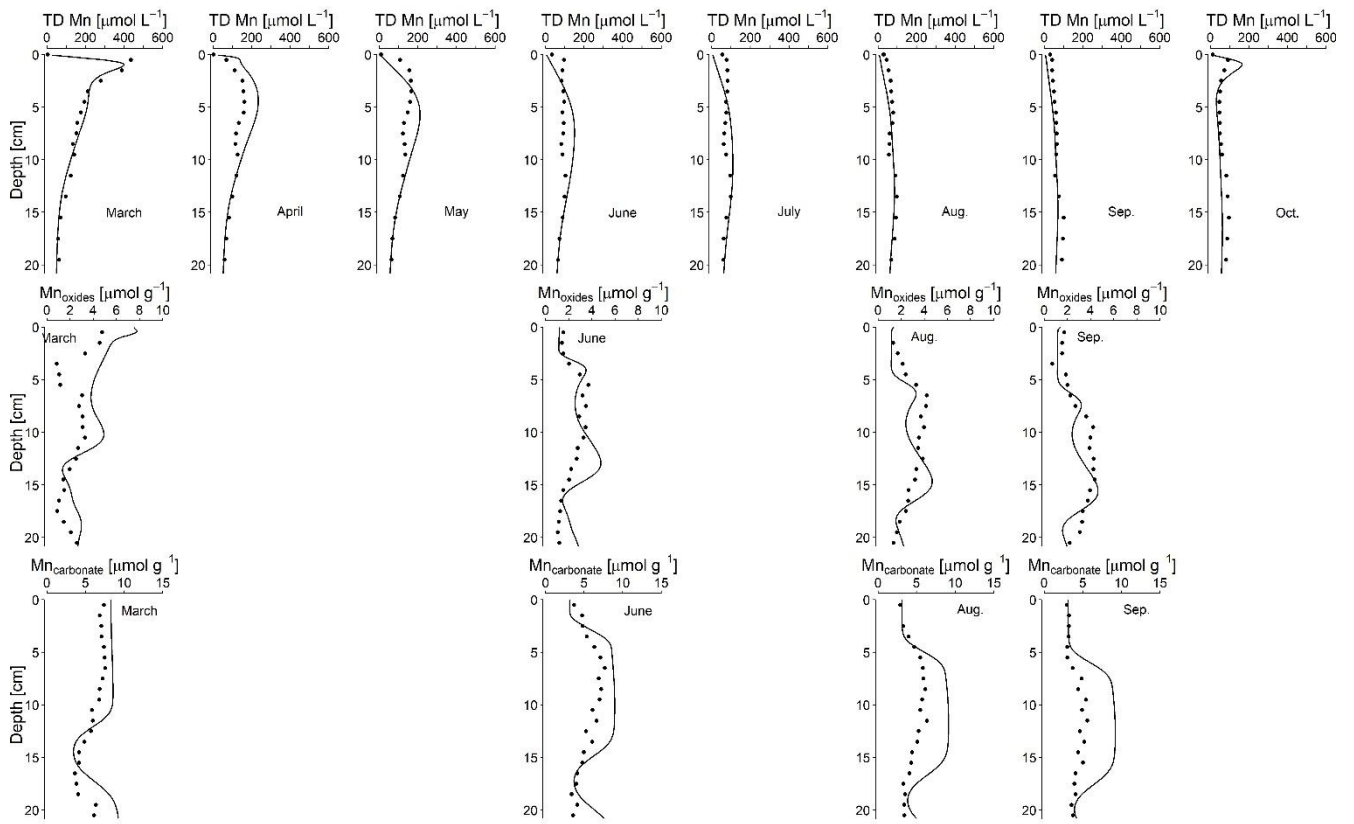
130   **Continuation of figure S11.**
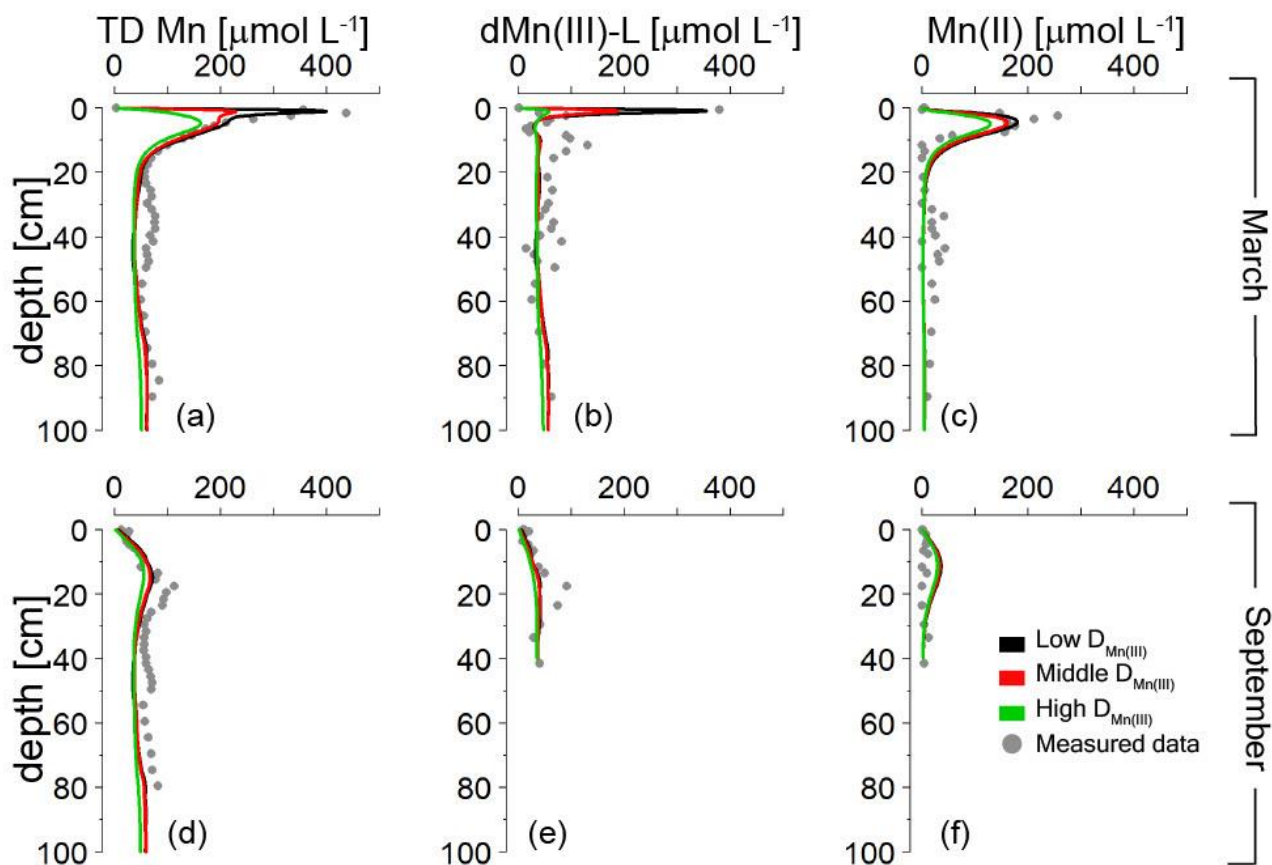
Figure S128: **Model runs with different diffusion coefficients for dissolved Mn(III). The diffusion coefficients used and the range of diffusion coefficients for dissolved organic matter given in literature can be found in Table S6. When the diffusion coefficient decreases, the peak of dissolved Mn(III)-L and total dissolved Mn near the sediment-water interface in March is no longer well described by the model. The diffusion coefficient does not have a large effect on the pore water profiles of Mn(II) and dMn(III)-L in September.**
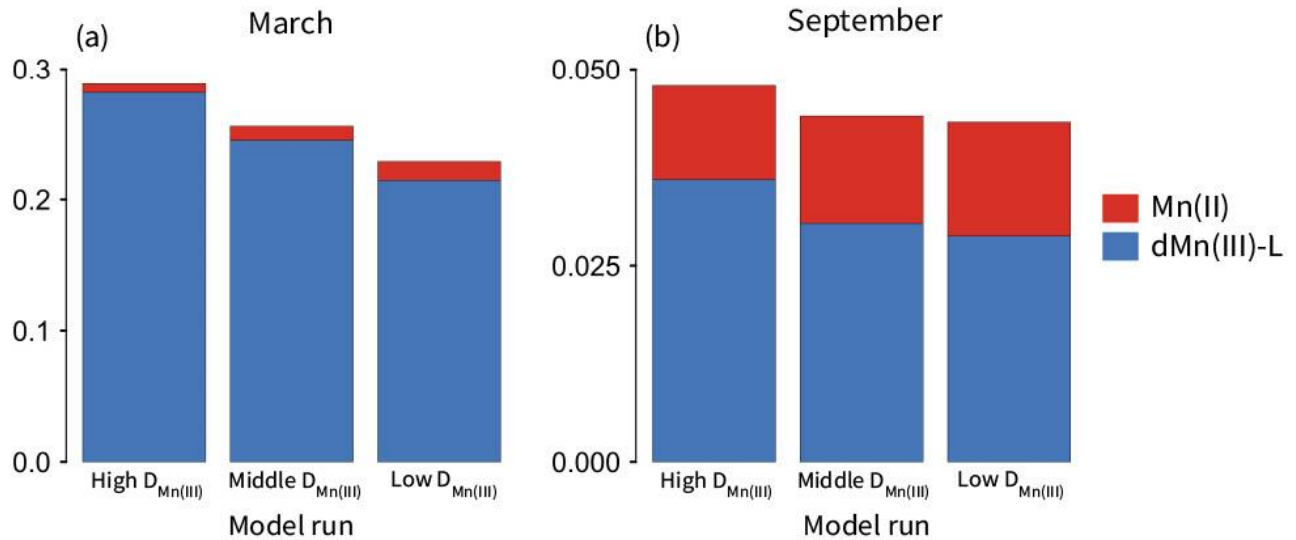
Figure S139: Variation in the benthic flux of dissolved Mn over the model runs with changing diffusion coefficient for dMn(III)-L (D$_{Mn(III)}$) in March (A) and September (B). Note the different y-axes for the different months. The figure shows that a lower diffusion coefficient for dMn(III)-L results in a lower benthic flux of total Mn and dMn(III)-L, but a slightly higher benthic flux of Mn(II). The values for the high, middle and low D$_{Mn(III)}$ can be found in Table S6.
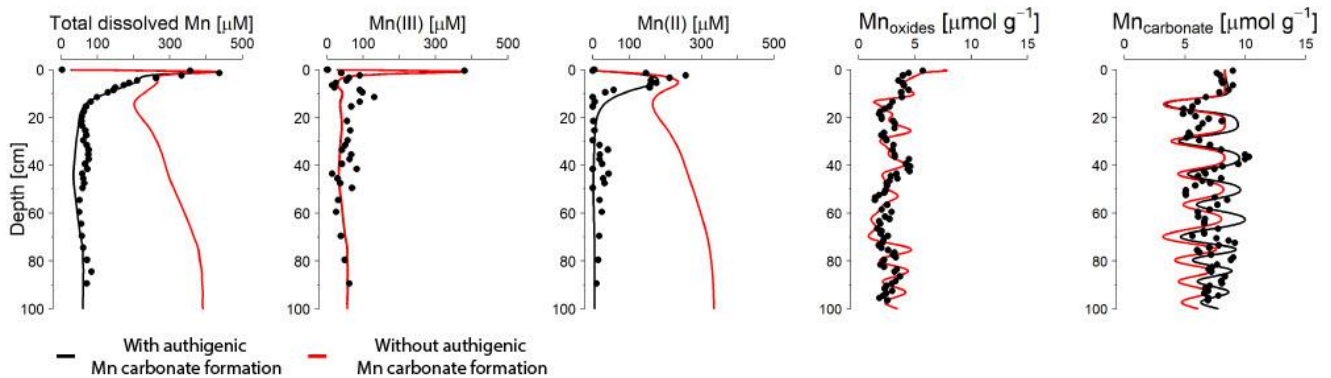
Figure S14: Model output when authigenic Mn carbonate precipitation is turned off in red versus the model base run in black. The difference in Mn carbonate concentrations between the model without Mn carbonate precipitation and the base run indicate the amount of Mn carbonate that, according to the model, has formed within the sediment

Table S1. Chemical species included in the model

Species	Notation
Solids	
Organic Matter[a]	$OM^{\alpha/\beta/\gamma}$
Iron oxides[a]	$Fe(OH)_3^{\alpha/\beta/\gamma}$
Iron monosulfide	FeS
Pyrite	FeS_2
Elemental Sulfur	S^0
Siderite	$FeCO_3$
Vivianite	$Fe_3(PO_4)_2$
Manganese oxide[b]	$MnO_2^{\alpha/\beta}$
Manganese carbonate	$MnCO_3$
Solutes	
Chloride	Cl^-
Oxygen	O_2
Nitrate	NO_3^-
Sulfate	SO_4^{2-}
Methane	CH_4
Dissolved iron	Fe^{2+}
Ammonium[c]	ΣNH_4^+
Hydrogen sulfide[c]	ΣH_2S
Phosphate[c]	ΣH_3PO_4
Dissolved Inorganic Carbon	DIC
Dissolved manganese (II)	Mn^{2+}
Dissolved manganese(III)-L	$Mn^{3+}\text{-L}\,Mn^{3+}$

[a] Consists of three types of species: reactive (α), less reactive (β) and non-reactive (γ)

[b] Consists of two types of species: reactive (α) and less reactive (β)

[c] Σ denotes that all species of an acid are included.

Table S2. Reaction pathways and stoichiometries implemented in the model

Primary redox reactions

$OM^{\alpha,\beta} + a\ O_2 \rightarrow a\ CO_2 + b\ NH_4^+ + c\ H_3PO_4 + a\ H_2O$	R1
$OM^{\alpha,\beta} + 0.8\ a\ NO_3 + 0.8\ a\ H^+ \rightarrow a\ CO_2 + b\ NH_4^+ + c\ H_3PO_4 + 0.4\ a\ N_2 + 1.4\ a\ H_2O$	R2
$OM^{\alpha,\beta} + 4a\ MnO_2{}^a + 2\ a\ H^+ \rightarrow 4a\ {\color{red}Mn^{3+} - L\text{Mn}^{3+}} + a\ CO_2 + b\ NH_4^+ + c\ H_3PO_4 + 2\ a\ H_2O$	R3
$OM^{\alpha,\beta} + 4a\ Fe(OH)_3{}^a + 4a\ \chi\ Fe_{ox}P + 12\ a\ H^+$ $\rightarrow 4a\ Fe^{2+} + a\ CO_2 + b\ NH_4^+ + (c + 4a\ \chi)H_3PO_4 + 13a\ H_2O$	R4
$OM^{\alpha,\beta} + 0.5a\ SO_4{}^{2-} + a\ H^+ \rightarrow a\ CO_2 + b\ NH_4^+ + c\ H_3PO_4 + 0.5a\ H_2S + a\ H_2O$	R5
$OM^{\alpha,\beta} \rightarrow 0.5a\ CO_2 + b\ NH_4^+ + c\ H_3PO_4 + 0.5a\ CH_4$	R6

Secondary and other reactions

$O_2 + Fe^{2+} + 8\ H_2O + 4\ \chi\ H_3PO_4 \rightarrow 4\ Fe(OH)_3{}^a + 4\ \chi\ Fe_{ox}P + 8\ CO_2$	R7
$2\ O_2 + FeS \rightarrow SO_4^{2-} + 2\ Fe^{2+} + 4\ H^+$	R8
$7\ O_2 + 2\ FeS_2 + 2\ H_2O + 4\ SO_4^{2-} \rightarrow 2\ Fe^{2+} + 4\ H^+$	R9
$2\ O_2 + H_2S + 2\ HCO_3^- \rightarrow SO_4^{2-} + 2\ CO_2 + 2\ H_2O$	R10
$2\ O_2 + CH_4 \rightarrow CO_2 + 2\ H_2O$	R11
$2\ Fe(OH)_3{}^a + 2\ \chi\ Fe_{ox}P + H_2S + 4\ CO_2 \rightarrow 2\ Fe^{2+} + 2\ \chi H_2PO_4^- + S^0 + 4\ HCO_3^- + 2\ H_2O$	R12
$Fe^{2+} + H_2S \rightarrow FeS + 2\ H^+$	R13
$FeS + H_2S \rightarrow FeS_2 + H_2$	R14
$SO_4^{2-} + CH_4 + CO_2 \rightarrow 2\ HCO_3^- + H_2S$	R15
$CH_4 + 8\ Fe(OH)_3{}^{a,\beta} + 8\ \chi\ Fe_{ox}P + 15\ H^+ \rightarrow HCO_3^- + 8\ Fe^{2+} + 8\ \chi H_2PO_4^- + 21\ H_2O$	R16
$4\ S^0 + 4\ H_2O \rightarrow 3\ H_2S + SO_4^{2-} + 2\ H^+$	R17
$FeS + S^0 \rightarrow FeS_2$	R18
$Fe(OH)_3{}^a + \chi\ Fe_{ox}P \rightarrow Fe(OH)_3{}^\beta + \chi\ H_2PO_4{}^-$	R19
$2\ Fe(OH)_3{}^\beta + 2\ \chi\ Fe_{ox}P + H_2S + 4\ CO_2 \rightarrow 2\ Fe^{2+} + 2\ \chi\ H_2PO_4{}^- + S^0 + 4\ HCO_3^- + 2\ H_2O$	R20
$2\ O_2 + NH_4^+ + 2\ HCO_3^- \rightarrow NO_3^- + 2\ CO_2 + 3\ H_2O$	R21
$3\ Fe^{2+} + 2\ H_2PO_4{}^- \rightarrow Fe_3(PO_4)_2 + 4\ H^+$	R22
$Fe^{2+} + CO_3{}^{2-} \rightarrow FeCO_3$	R23
$FeCO_3 + H_2S \rightarrow FeS + CO_2 + H_2O$	R24
$Fe_3(PO_4)_2 + 3\ H_2S \rightarrow 2\ FeS + 2\ HPO_4^- + 4\ H^+$	R25
$Mn^{2+} + HCO_3^- + OH^- \rightarrow MnCO_3 + H_2O$	R26
$4\ Mn^{2+} + O_2 + 4\ H^+ + L \rightarrow 4\ Mn^{3+} - L + 2\ H_2O$	R27

$MnO_2^{\alpha,\beta} + Fe^{2+} + H_2O + H^+ + L \rightarrow Fe(OH)_3^{\alpha} + Mn^{3+} - L$	R28
$MnO_2^{\alpha} + H_2S + + 2\,H^+ + L \rightarrow S^0 + Mn^{3+} - L + 2\,H_2O$	R29
$MnO_2^{\alpha} \rightarrow MnO_2^{\beta}$	R30
$MnO_2^{\beta} + H_2S + + 2\,H^+ + L \rightarrow S^0 + Mn^{3+} - L + 2\,H_2O$	R31
$4\,MnO_2^{\alpha,\beta} + CH_4 + 7\,H^+ \rightarrow 4\,Mn^{2+} + HCO_3^- + 5\,H_2O$	R32
$4\,Mn^{3+} - L + 2\,O_2 + 4\,H^+ \rightarrow 4\,MnO_2^{\alpha} + 2\,H_2O + L$	R33
$Mn^{3+} - L + H_2S \rightarrow S^0 + Mn^{2+} + L$	R34
$Mn^{3+} - L + Fe^{2+} + 3\,H_2O \rightarrow Mn^{2+} + Fe(OH)_3^{\alpha} + 3\,H^+ + L$	R35
$4\,Mn^{3+} - L + OM^{\alpha} + H_2O \rightarrow 4\,Mn^{2+} + CO_2 + 3\,H^+ + L$	R36

Organic matter is of the form $((CH_2O)_a\,(NH_4^+)_b\,(H_3PO_4)_c$, where a=1, b= 1/15.45 and c = 106/1. α, β, & γ describe different fractions (i.e. highly reactive, less reactive and refractory). χ describes the P:Fe ratios of $Fe(OH)_3$ and has a value of 0.3 in the model.

160

Table S3. Reaction equations implemented in the model

Primary redox reaction equations	
$R1 = k_{\alpha,\beta}\,OM^{\alpha,\beta} \left(\dfrac{[O_2]}{K_{m,O_2}+[O_2]}\right)\left(\dfrac{\cancel{[O_2]}}{\cancel{K_{m,O_2}+[O_2]}}\right)$	E1
$R2 = k_{\alpha,\beta}\,OM^{\alpha,\beta} \left(\dfrac{[NO_3^-]}{K_{m,NO_3^-}+[NO_3^-]}\right)\left(\dfrac{K_{m,O_2}}{K_{m,O_2}+[O_2]}\right)\left(\dfrac{\cancel{[NO_3^-]}}{\cancel{K_{m,NO_3^-}+[NO_3^-]}}\right)\left(\dfrac{\cancel{[O_2]}}{\cancel{K_{m,O_2}+[O_2]}}\right)$	E2
$R3 = k_{\alpha,\beta}\,OM^{\alpha,\beta} \left(\dfrac{[MnO_2]}{K_{m,MnO_2}+[MnO_2]}\right)\left(\dfrac{K_{m,NO_3^-}}{K_{m,NO_3^-}+[NO_3^-]}\right)\left(\dfrac{K_{m,O_2}}{K_{m,O_2}+[O_2]}\right)\left(\dfrac{\cancel{[MnO_2]}}{\cancel{K_{m,MnO_2}+[MnO_2]}}\right)\left(\dfrac{\cancel{[NO_3^-]}}{\cancel{K_{m,NO_3^-}+[NO_3^-]}}\right)\left(\dfrac{\cancel{[O_2]}}{\cancel{K_{m,O_2}+[O_2]}}\right)$	E3
$R4 =$ $k_{\alpha,\beta}\,OM^{\alpha,\beta} \left(\dfrac{[Fe(OH)_3]}{K_{m,Fe(OH)_3}+[Fe(OH)_3]}\right)\left(\dfrac{K_{m,MnO_2}}{K_{m,MnO_2}+[MnO_2]}\right)\left(\dfrac{K_{m,NO_3^-}}{K_{m,NO_3^-}+[NO_3^-]}\right)\left(\dfrac{K_{m,O_2}}{K_{m,O_2}+[O_2]}\right)\left(\dfrac{\cancel{[Fe(OH)_3]}}{\cancel{K_{m,Fe(OH)_3}+[Fe(OH)_3]}}\right)\left(\dfrac{\cancel{[MnO_2]}}{\cancel{K_{m,MnO_2}+[Mn\ldots]}}\right)$	E4
$R5 =$	E5

$$k_{\alpha,\beta}\, \mathrm{OM}^{\alpha,\beta}\left(\frac{[SO_4^{2-}]}{K_{m,SO_4^{2-}}+[SO_4^{2-}]}\right)\left(\frac{K_{m,Fe(OH)_3}}{K_{m,Fe(OH)_3}+[Fe(OH)_3]}\right)\left(\frac{K_{m,MnO_2}}{K_{m,MnO_2}+[MnO_2]}\right)$$

$$*\left(\frac{K_{m,NO_3^-}}{K_{m,NO_3^-}+[NO_3^-]}\right)\left(\frac{K_{m,O_2}}{K_{m,O_2}+[O_2]}\right)\cancel{\left(\frac{[Fe(OH)_3]}{K_{m,Fe(OH)_3}+[Fe(OH)_3]}\right)}\cancel{\left(\frac{[MnO_2]}{K_{m,MnO_2}+[MnO_2]}\right)}$$

$$*\cancel{\left(\frac{[NO_3^-]}{K_{m,NO_3^-}+[NO_3^-]}\right)}\cancel{\left(\frac{[O_2]}{K_{m,O_2}+[O_2]}\right)}$$

| | E6 |

$$R6 =$$

$$k_{\alpha,\beta}\, \mathrm{OM}^{\alpha,\beta}\left(\frac{K_{m,SO_4^{2-}}}{K_{m,SO_4^{2-}}+[SO_4^{2-}]}\right)\left(\frac{K_{m,Fe(OH)_3}}{K_{m,Fe(OH)_3}+[Fe(OH)_3]}\right)\left(\frac{K_{m,MnO_2}}{K_{m,MnO_2}+[MnO_2]}\right)$$

$$*\left(\frac{K_{m,NO_3^-}}{K_{m,NO_3^-}+[NO_3^-]}\right)\left(\frac{K_{m,O_2}}{K_{m,O_2}+[O_2]}\right)\cancel{\left(\frac{K_{m,SO_4^{2-}}}{K_{m,SO_4^{2-}}+[SO_4^{2-}]}\right)}\cancel{\left(\frac{[Fe(OH)_3]}{K_{m,Fe(OH)_3}+[Fe(OH)_3]}\right)}\cancel{\left(\frac{[MnO_2]}{K_{m,MnO_2}+[MnO_2]}\right)}$$

$$*\cancel{\left(\frac{[NO_3^-]}{K_{m,NO_3^-}+[NO_3^-]}\right)}\cancel{\left(\frac{[O_2]}{K_{m,O_2}+[O_2]}\right)}$$

Secondary redox and other reaction equations

Equation	ID
$R7 = k_1\,[O_2]\,[Fe^{2+}]$	E7
$R8 = k_2\,[O_2]\,[FeS]$	E8
$R9 = k_3\,[O_2]\,[FeS_2]$	E9
$R10 = k_4\,[O_2]\,[\sum H_2S]$	E10
$R11 = k_5\,[O_2]\,[CH_4]$	E11
$R12 = k_6\,\left[Fe(OH)_3{}^{\alpha}\right]\,[\sum H_2S]$	E12
$R13 = k_7\,[Fe^{2+}]\,[\sum H_2S]$	E13
$R14 = k_8\,[FeS]\,[\sum H_2S]$	E14
$R15 = k_9\,[SO_4^{2-}]\,[CH_4]$	E15

$R16 = k_{10} \left[Fe(OH)_3{}^{\alpha,\beta} \right] [CH_4]$	E16
$R17 = k_{11} \left[S^0 \right]$	E17
$R18 = k_{12} \left[FeS \right] \left[S^0 \right]$	E18
$R19 = k_{13} \left[Fe(OH)_3{}^{\alpha} \right]$	E19
$R20 = k_{14} \left[Fe(OH)_3{}^{\beta} \right] \left[\sum H_2S \right]$	E20
$R21 = k_{15} \left[O_2 \right] \left[NH_4^+ \right]$	E21
$R22 = k_{16} \left[Fe^{2+} \right] \left[HPO_4^{2-} \right]$	E22
$R23 = k_{17} \left[Fe^{2+} \right] \left[HCO_3^- \right]$	E23
$R24 = k_{18} \left[FeCO_3 \right] \left[\sum H_2S \right]$	E24
$R25 = k_{19} \left[Fe_3(PO_4)_2 \right] \left[\sum H_2S \right]$	E25
$R26 = k_{20} \left[Mn^{2+} \right] \left[HCO_3^- \right]$	E26
$R27 = k_{21} \left[Mn^{2+} \right] \left[O_2 \right]$	E27
$R28 = k_{22} \left[MnO_2 \,\text{~~Mn(OH)}_4\text{~~}{}^{\alpha,\beta} \right] \left[Fe^{2+} \right]$	E28
$R29 = k_{23} \left[MnO_2 \,\text{~~Mn(OH)}_4\text{~~}{}^{\alpha} \right] \left[\sum H_2S \right]$	E29
$R30 = k_{24} \left[MnO_2 \,\text{~~Mn(OH)}_4\text{~~}{}^{\alpha} \right]$	E30
$R31 = k_{25} \left[MnO_2 \,\text{~~Mn(OH)}_4\text{~~}{}^{\beta} \right] \left[\sum H_2S \right]$	E31

$R32 = k_{26} \left[MnO_2 \text{~~Mn(OH)}_4\text{~~}^{\alpha,\beta} \right] [CH_4]$	E32
$R33 = k_{27} \left[Mn^{3+} - L\text{~~Mn}^{3+}\text{~~} \right] [O_2]$	E33
$R34 = k_{28} \left[Mn^{3+} - L\text{~~Mn}^{3+}\text{~~} \right] [\Sigma H_2S]$	E34
$R35 = k_{29} \left[\text{~~Mn}^{3+}\text{~~} Mn^{3+} - L \right] [Fe^{2+}]$	E35
$R36 = k_{30} \left[Mn^{3+} - L \right][OM^{\alpha}] \text{~~} k_{30} [CO_2][H_2]\text{~~}$	E36
$R37 = k_{31} [OM^{\alpha}]$	E37
$R38 = k_{32} [NO_3^-][CH_4]$	E38
$R39 = k_{33} [CO_2][H_2] \left(\frac{K_{m,SO_4^{2-}}}{K_{m,SO_4^{2-}}+[SO_4^{2-}]} \right) \left(\frac{K_{m,Fe(OH)_3}}{K_{m,Fe(OH)_3}+[Fe(OH)_3]} \right) \left(\frac{K_{m,MnO_2}}{K_{m,MnO_2}+[MnO_2]} \right) *$ $\left(\frac{K_{m,NO_3^-}}{K_{m,NO_3^-}+[NO_3^-]} \right) \left(\frac{K_{m,O_2}}{K_{m,O_2}+[O_2]} \right) \text{~~} k_{33}[Mn^{3+}][OM^{\alpha}]\text{~~}$	E39

Table S4. Reaction parameters used in the model

Parameter	Value	Unit	Source	Values in literature
$k_{\alpha}*$	1.62	yr^{-1}	a, b	0.05 – 1.62
$k_{\beta}*$	0.0086	yr^{-1}	b, d	0.0025 - 0.0086
K_{O_2}	20	$\mu mol\ L^{-1}$	c	1 – 30
$K_{NO_3^-}$	20	$\mu mol\ L^{-1}$	c	4 – 80
$K_{MnO_2 \text{~~Mn(OH)}_4\text{~~}}$	32	$\mu mol\ L^{-1}$	c	4 – 32
$K_{Fe(OH)_3}$	65	$\mu mol\ L^{-1}$	c	65 – 100
$K_{SO_4^{2-}}$	1.6	$\mu mol\ L^{-1}$	c	1.6
k_1 (E7)	$1.4*10^5$	$mmol\ yr^{-1}$	c	$1.4*10^5$
k_2 (E8)	300	$mmol\ yr^{-1}$	c	300

k_3 (E9)	1	mmol yr^{-1}	c	1
k_4 (E10)	160	mmol yr^{-1}	c	160
k_5 (E11)	100	mmol yr^{-1}	c	107
k_6 (E12)	80	mmol yr^{-1}	c, g, i	8 - 100
k_7 (E13)	11840	mmol yr^{-1}	b, d	100 - 14800
k_8 (E14)	0.0003	mmol yr^{-1}	e, i	0.0003 – 0.0074
k_9 (E15)	1.344	mmol yr^{-1}	c, g	10 (c) – 120 (g)
k_{10} (E16)	3.04×10^{-6}	mmol yr^{-1}	g, i	1.6×10^{-7} – 0.0074
k_{11} (E17)	3	yr^{-1}	f	3
k_{12} (E18)	0.1	mmol yr^{-1}	f, g	0.001 - 7
k_{13} (E19)	0.1	yr^{-1}		model constrained
k_{14} (E20)	0.444	mmol yr^{-1}	c, j	0.004 – 100
k_{15} (E21)	19500	mmol yr^{-1}	c, d	5000 – 39000
k_{16} (E22)	0.052	mmol yr^{-1}		model constrained
k_{17} (E23)	0.000351	mmol yr^{-1}	i	0.0027
k_{18} (E24)	0.0008	mmol yr^{-1}		model constrained
k_{19} (E25)	8×10^{-4}	mmol yr^{-1}	i	8×10^{-4}
k_{20} (E26)	0.05565	mmol yr^{-1}	k	0.265
k_{21} (E27)	15000	mmol yr^{-1}	c	800 - 20000
k_{22} (E28)	2.652	mmol yr^{-1}	f, k	0.002 - 2
k_{23} (E29)	1	mmol yr^{-1}	c	< 100000 (20)
k_{24} (E30)	1.8	yr^{-1}	f	1.8
k_{25} (E31)	0.02	mmol yr^{-1}	c	< 100000 (20)
k_{26} (E32)	0.000019	mmol yr^{-1}	k	0.0017
k_{27} (E33)	144	mmol yr^{-1}		model constrained
k_{28} (E34)	64	mmol yr^{-1}		model constrained
k_{29} (E35)	0.025	mmol yr^{-1}		model constrained
k_{30} (E36)k_{30} (E36)	2.5×10^{-4}0.03675	mmol yr^{-1}yr^{-1}		model constrainedmodel constrained
k_{31} (E37)	0.15	yr^{-1}		model constrained
k_{32} (E38)	0.5	mmol yr^{-1}		model constrained

~~k~~$_{33}$~~(E39)~~k$_{33}$(E39)	0.03675~~2.5*10^{-4}~~	yr^{-1}~~mmol yr^{-1}~~		model constrained~~model constrained~~

a) Moodley et al. (2005); b) Reed et al. (2011a) c) Van Cappellen & Wang (1996); d) Reed et al. (2016); e) Rickard (1997); f) Berg et al. (2003); g) Rooze et al. (2016); h) Egger et al. (2016a); i) Egger et al. (2016b); j) Lenstra et al. (2018)

165

*Following the approach of Reed et al. (2011b), we have assumed different reactivities of the organic matter towards the electron acceptors. The following factors have been used for the α fraction: $O_2 = 1$, $NO_3 = 3$, $MnO_2 = 2.8$, $Fe(OH)_3 = 0.3$, $SO_4^{2-} = 1.7$, methanogenesis = 0.5; for the β fraction the following factors have been used: $O_2 = 1$, $NO_3^- = 3$, $MnO_2 = 1$, $Fe(OH)_3 = 0.3$, $SO_4^{2-} = 1$, methanogenesis = 3.

170

Table S5. Environmental parameters used in the model. Values of porosity, temperature, salinity and the sedimentation rate are based on data for the study site.

Parameter	Symbol	Value	Unit
Porosity at surface	ϕ_0	0.944	vol/vol
Porosity at depth	ϕ_∞	0.888	-
Porosity e-folding distance	g	60	cm
Sediment density	r	2.65	g cm^{-3}
Temperature	T	8.4	˚C
Salinity	S	35	-
Pressure	P	5.5	bar
Tortuosity	q^2	$1 - 2\ln(\phi)$	-
Molecular diffusion coefficient corrected for tortuosity	D'	$D' = \dfrac{D_m}{\theta^2}$	cm^{-2} yr^{-1}
Sediment accumulation rate**	F_{Sed}	**	g cm^{-2} yr^{-1}
Advective velocity at surface	n_0	$\dfrac{F_{sed}}{\rho(1-\varphi_0)}$	cm yr^{-1}
Advective velocity at depth	n_∞	$\dfrac{F_{sed}}{\rho(1-\varphi_\infty)}$	cm yr^{-1}
** Sedimentation rate variations over the years			

Year	December – July	July - December	Unit
0 – 60	2.97	2.97	g cm^{-2} yr^{-1}
60 – 75	0.69	3.93	g cm^{-2} yr^{-1}
75 – 80	3.93	2.00	g cm^{-2} yr^{-1}

175 **Table S6. The various diffusion coefficients used for Mn(III) (D$_{Mn(III)}$) to evaluate the effect of the choice of the diffusion coefficient for Mn(III) when it forms a complex with an organic ligand.**

Name	Scenario	Value	Range in literature	Sources
High D$_{Mn(III)}$	DMn(III) = DMn(II) As calculated by reactran package	132.6 cm^2 yr^{-1}	-	*a*
Middle D$_{Mn(III)}$	DMn(III) is within the range of diffusion coefficients for dissolved organic matter	33.1 cm^2 yr^{-1}	22.7 – 81 cm^2 yr^{-1}	*b, c*
Low D$_{Mn(III)}$	DMn(III) is constrained by the model, by fitting Mn(III) to the collected data. This is the DMn(III) that is used in the model throughout the paper.	16.6 cm^2 yr^{-1}	-	

Sources: *a*) Soetaert & Meysman (2012); *b*) Burdige et al. (1999); *c*) Burdige et al. (2004)

180

Table S7. Boundary conditions of solids and solutes at the sediment-water interface in the model. For the time-dependent fluxes of $OM^{\alpha,\beta,\gamma}, Fe(OH)_3^{\alpha,\beta,\gamma}, MnO_2^{\alpha,\beta}$ and $MnCO_3$ and concentration of O$_2$ the minimum and maximum fluxes and concentrations are given. For all chemical species, a zero-gradient boundary condition was specified at the bottom of the model domain.

Solids	Flux at sediment-water interface	Unit
FeS	0.4 * 10^{-4}	mol m^{-2} yr^{-1}

FeS_2	0		mol m^{-2} yr^{-1}
S^0	0		mol m^{-2} yr^{-1}
$FeCO_3$	2		mol m^{-2} yr^{-1}
$Fe_3(PO_4)_2$	0		mol m^{-2} yr^{-1}
	Min	**Max**	
OM[a]	9.51	52.31	mol m^{-2} yr^{-1}
OM[b]	45.36	72.58	mol m^{-2} yr^{-1}
OM[g]	0.001	0.001	mol m^{-2} yr^{-1}
$Fe(OH)_3$[a]	0.0028	6.44	mol m^{-2} yr^{-1}
$Fe(OH)_3$[b]	3.28	4.68	mol m^{-2} yr^{-1}
$Fe(OH)_3$[g]	0	0	mol m^{-2} yr^{-1}
MnO_2[a]	0.0108	0.081	mol m^{-2} yr^{-1}
MnO_2[b]	0.0235	0.216	mol m^{-2} yr^{-1}
$MnCO_3$	0.0624	0.163	mol m^{-2} yr^{-1}
Solutes	**Bottom water concentrations**		**Unit**
	Min	**Max**	
O_2	0	0.205	mmol L^{-1}
ΣH_2S	0	0.111	mmol L^{-1}
Cl^-	532		mmol L^{-1}
NO_3^-	0		mmol L^{-1}
SO_4^{2-}	27.49		mmol L^{-1}
CH_4	0		mmol L^{-1}
Fe^{2+}	0		mmol L^{-1}
ΣNH_4^+	0		mmol L^{-1}
ΣHPO_4^{2-}	0		mmol L^{-1}
DIC	3		mmol L^{-1}
Mn^{2+}	0		mmol L^{-1}
Mn^{3+}	0		mmol L^{-1}

185

References

Berg, P., Rysgaard, S., & Thamdrup, B. O. : Dynamic Modeling of Early Diagenesis and Nutrient Cycling. A Case Study in an Arctic Marine Sediment. Am. J. Sci., 303, 905–955, 2003.

Boudreau, B. P.: Diagenetic models and their implementation : modelling transport and reactions in aquatic sediments Modelling Transport and Reactions in Aquatic Sediments. Springer Berlin Heidelberg. https://doi.org/10.1007/978-3-642-60421-8, 1997.

Boudreau, P.: A Method-of-Lines Code For Carbon and Nutrient Diagenesis in Aquatic Sediments. Comput. Geosci., 22(5), 479–496, 1996.

Burdige, D. J., Berelson, W. M., Coale, K. H., McManus, J., & Johnson, K. S.: Fluxes of dissolved organic carbon from California continental margin sediments. Geochim. Cosmochim. Ac., 63(10), 1507–1515, 1999.

Burdige, D. J., Kline, S. W., & Chen, W.: Fluorescent dissolved organic matter in marine sediment pore waters. Mar. Chem., 89, 289–311. https://doi.org/10.1016/j.marchem.2004.02.015, 2004.

Cline, J. D.: Spectrophotometric Determination of Hydrogen Sulfide in Natural Waters. Limnol. Oceanogr., 14(3), 454–458. https://doi.org/10.4319/lo.1969.14.3.0454, 1969.

Egger, M., Kraal, P., Jilbert, T., Sulu-gambari, F., Sapart, C. J., & Röckmann, T.: Anaerobic oxidation of methane alters sediment records of sulfur , iron and phosphorus in the Black Sea. Biogeosciences, 5333–5355. https://doi.org/10.5194/bg-13-5333-2016, 2016.

Egger, M., Lenstra, W., Jong, D., Meysman, F. J. R., Sapart, C. J., Van Der Veen, C., Röckmann, T., Gonzalez, S., & Slomp, C. P.: Rapid sediment accumulation results in high methane effluxes from coastal sediments. PLoS ONE, 11(8), 1–22. https://doi.org/10.1371/journal.pone.0161609, 2016.

Froelich, P. N., Klinkhammer, G. P., Bender, M. L., Luedtke, N. A., Heath, G. R., Cullen, D., Dauphin, P., Hammond, D., & Hartman, B.: Early oxidation of organic matter in pelagic sediments of the eastern equatorial Atlantic : suboxic diagenesis. Geochim. Cosmochim. Ac., 43, 1075–1090, 1979.

Hagens, M., Slomp, C. P., Meysman, F. J. R., Seitaj, D., Harlay, J., Borges, A. V., & Middelburg, J. J.: Biogeochemical processes and buffering capacity concurrently affect acidification in a seasonally hypoxic coastal marine basin. Biogeosciences, 12(5), 1561–1583. https://doi.org/10.5194/bg-12-1561-2015, 2015.

Hulth, S., Aller, R. C., & Gilbert, F.: Coupled anoxic nitrification / manganese reduction in marine sediments. Geochim. Cosmochim. Ac., 63(1), 49–66, 1999.

Karolewski, J. S., Sutherland, K. M., Hansel, C. M., & Wankel, S. D.: An isotopic study of abiotic nitrite oxidation by ligand-bound manganese (III). Geochim. Cosmochim. Ac., 293, 365–378. https://doi.org/10.1016/j.gca.2020.11.004, 2021.

Lenstra, W. K., Egger, M., Helmond, N. A. G. M. Van, Kritzberg, E., Conley, D. J. & Slomp, C.P.: Large variations in iron input to an oligotrophic Baltic Sea estuary : impact on sedimentary phosphorus burial. Biogeosciences, 6979–6996, 2018.

Lenstra, W. K., Klomp, R., Molema, F., Behrends, T., & Slomp, C. P.: A sequential extraction procedure for particulate manganese and its application to coastal marine sediments. Chem. Geol., 584(June), 120538. https://doi.org/10.1016/j.chemgeo.2021.120538, 2021.

Meysman, F. J. R., Boudreau, B. P., & Middelburg, J. J.: Modeling reactive transport in sediments subject to bioturbation and compaction. Geochim. Cosmochim. Ac., 69(14), 3601–3617. https://doi.org/10.1016/j.gca.2005.01.004, 2005.

225 Moodley, L., Middelburg, J. J., Herman, P. M. J., Soetaert, K., & de Lange, G. J.: Oxygenation and organic-matter preservation in marine sediments : Direct experimental evidence from ancient organic carbon – rich deposits. Geology, 11, 889–892. https://doi.org/10.1130/G21731.1, 2005.

Reed, D. C., Gustafsson, B. G., & Slomp, C. P.: Shelf-to-basin iron shuttling enhances vivianite formation in deep Baltic Sea sediments. Earth and Planetary Science Letters, 434, 241–251. https://doi.org/10.1016/j.epsl.2015.11.033, 2016.

230 Reed, D. C., Slomp, C. P., & de Lange, G. J.: A quantitative reconstruction of organic matter and nutrient diagenesis in Mediterranean Sea sediments over the Holocene. Geochim. Cosmochim. Ac., 75(19), 5540–5558. https://doi.org/10.1016/j.gca.2011.07.002, 2011.

Reed, D. C., Slomp, C. P., & Gustafsson, B. G.: Sedimentary phosphorus dynamics and the evolution of bottom-water hypoxia: A coupled benthic-pelagic model of a coastal system. Limnol. Oceanogr., 56(3), 1075–1092.
235 https://doi.org/10.4319/lo.2011.56.3.1075, 2011.

Rickard, D.: Kinetics of pyrite formation by the H2S oxidation of iron (II) monosulfide in aqueous solutions between 25 and 125 ° C : The rate equation. Geochim. Cosmochim. Ac., 61(1), 115–134, 1997.

Rooze, J., Egger, M., Tsandev, I., & Slomp, C. P.: Iron-dependent anaerobic oxidation of methane in coastal surface sediments: Potential controls and impact. Limnol. Oceanogr., 61(1), S267–S282. https://doi.org/10.1002/lno.10275, 2016.

240 Soetaert, K., & Meysman, F.: Environmental Modelling & Software Reactive transport in aquatic ecosystems : Rapid model prototyping in the open source software R. Environ. Model. Softw., 32, 49–60. https://doi.org/10.1016/j.envsoft.2011.08.011, 2012.

Solórzano, L.: Determination of Ammonia in Natural Waters by the Phenolhypochlorite Method. Limnol. Oceanogr., 14(September), 799–801. https://doi.org/10.4319/ lo.1969.14.5.0799, 1968.

245 Thamdrup, B., & Dalsgaard, T.: The fate of ammonium in anoxic manganese oxide-rich marine sediment. Geochim. Cosmochim. Ac., 64(24), 4157–4164, 2000.

Van Cappellen, P., & Wang, Y.: Cycling of iron and manganese in surface sediments: a general theory for the coupled transport and reaction of carbon, oxygen, nitrogen, sulfur, iron and manganese. Am J Sci, 296(March), 197–243, 1996.

Żygadłowska, O. M., Venetz, J., Klomp, R., Lenstra, W. K., Van Helmond, N. A. G. M., Röckmann, T., Wallenius, A. J.,
250 Dalcin Martins, P., Veraart, A. J., Jetten, M. S. M., & Slomp, C. P.: Pathways of methane removal in the sediment and water column of a seasonally anoxic eutrophic marine basin. Front Mar. Sci., January, 1–15. https://doi.org/10.3389/fmars.2023.1085728, 2023.

Żygadłowska, O. M., van Helmond, N. A. G. M., Lenstra, W. K., Klomp, R., Accou, R., Puyk, R., Dickson, A. J., Jetten, M. S. M., & Slomp, C. P.: Seasonal euxinia in a coastal basin: Impact on sedimentary molybdenum enrichments and isotope
255 signatures. Chem. Geol., 670(September), 122297. https://doi.org/10.1016/j.chemgeo.2024.122297, 2024a.

Żygadłowska, O. M., Venetz, J., Lenstra, W. K., Van Helmond, N. A. G. M., Klomp, R., Röckmann, T., & Slomp, C. P.: Ebullition drives high methane emissions from a eutrophic coastal basin. Geochim. Cosmochim. Ac., 384, 1–13. https://doi.org/10.1016/j.gca.2024.08.028, 2024b.

Berg, P., Rysgaard, S., & Thamdrup, B. O. (2003). Dynamic Modeling of Early Diagenesis and Nutrient Cycling. A Case
260 Study in an Arctic Marine Sediment. American Journal of Science, 303, 905–955.

Boudreau, B. P. (1997). Diagenetic models and their implementation : modelling transport and reactions in aquatic sediments Modelling Transport and Reactions in Aquatic Sediments. Springer Berlin Heidelberg. https://doi.org/10.1007/978-3-

642-60421-8

Boudreau, P. (1996). A Method of Lines Code For Carbon and Nutrient Diagenesis in Aquatic Sediments. *Computers & Geoscience*, 22(5), 479–496.

Burdige, D. J., Berelson, W. M., Coale, K. H., McManus, J., & Johnson, K. S. (1999). Fluxes of dissolved organic carbon from California continental margin sediments. *Geochimica et Cosmochimica Acta*, 63(10), 1507–1515.

Burdige, D. J., Kline, S. W., & Chen, W. (2004). Fluorescent dissolved organic matter in marine sediment pore waters. *Marine Chemistry*, 89, 289–311. https://doi.org/10.1016/j.marchem.2004.02.015

Egger, M., Kraal, P., Jilbert, T., Sulu-gambari, F., Sapart, C. J., & Röckmann, T. (2016a). Anaerobic oxidation of methane alters sediment records of sulfur, iron and phosphorus in the Black Sea. *Biogeosciences*, 5333–5355. https://doi.org/10.5194/bg-13-5333-2016

Egger, M., Lenstra, W., Jong, D., Meysman, F. J. R., Sapart, C. J., Van Der Veen, C., Röckmann, T., Gonzalez, S., & Slomp, C. P. (2016b). Rapid sediment accumulation results in high methane effluxes from coastal sediments. *PLoS ONE*, 11(8), 1–22. https://doi.org/10.1371/journal.pone.0161609

Froelich, P. N., Klinkhammer, G. P., Bender, M. L., Luedtke, N. A., Heath, G. R., Cullen, D., Dauphin, P., Hammond, D., & Hartman, B. (1979). Early oxidation of organic matter in pelagic sediments of the eastern equatorial Atlantic : suboxic diagenesis. *Geochimica et Cosmochimica Acta*, 43, 1075–1090.

Lenstra, W. K., Egger, M., Helmond, N. A. G. M. Van, Kritzberg, E., & Conley, D. J. (2018). Large variations in iron input to an oligotrophic Baltic Sea estuary : impact on sedimentary phosphorus burial. *Biogeosciences*, 6979–6996.

Meysman, F. J. R., Boudreau, B. P., & Middelburg, J. J. (2005). Modeling reactive transport in sediments subject to bioturbation and compaction. *Geochimica et Cosmochimica Acta*, 69(14), 3601–3617. https://doi.org/10.1016/j.gca.2005.01.004

Moodley, L., Middelburg, J. J., Herman, P. M. J., Soetaert, K., & de Lange, G. J. (2005). Oxygenation and organic matter preservation in marine sediments : Direct experimental evidence from ancient organic carbon—rich deposits. *Geology*, 11, 889–892. https://doi.org/10.1130/G21731.1

Reed, D. C., Gustafsson, B. G., & Slomp, C. P. (2016). Shelf to basin iron shuttling enhances vivianite formation in deep Baltic Sea sediments. *Earth and Planetary Science Letters*, 434, 241–251. https://doi.org/10.1016/j.epsl.2015.11.033

Reed, D. C., Slomp, C. P., & de Lange, G. J. (2011a). A quantitative reconstruction of organic matter and nutrient diagenesis in Mediterranean Sea sediments over the Holocene. *Geochimica et Cosmochimica Acta*, 75(19), 5540–5558. https://doi.org/10.1016/j.gca.2011.07.002

Reed, D. C., Slomp, C. P., & Gustafsson, B. G. (2011b). Sedimentary phosphorus dynamics and the evolution of bottom-water hypoxia: A coupled benthic-pelagic model of a coastal system. *Limnology and Oceanography*, 56(3), 1075–1092. https://doi.org/10.4319/lo.2011.56.3.1075

Rickard, D. (1997). Kinetics of pyrite formation by the H2S oxidation of iron (II) monosulfide in aqueous solutions between 25 and 125 ° C : The rate equation. *Geochimica et Cosmochimica Acta*, 61(1), 115–134.

Rooze, J., Egger, M., Tsandev, I., & Slomp, C. P. (2016). Iron-dependent anaerobic oxidation of methane in coastal surface sediments: Potential controls and impact. *Limnology and Oceanography*, *61*(1), S267–S282. https://doi.org/10.1002/lno.10275

Soetaert, K., & Meysman, F. (2012). Environmental Modelling & Software Reactive transport in aquatic ecosystems : Rapid model prototyping in the open source software R. *Environmental Modelling and Software*, *32*, 49–60. https://doi.org/10.1016/j.envsoft.2011.08.011

Soetaert, K., Petzoldt, T., & Meysman, F. (2010). *marelac : Tools for Aquatic Sciences*.

Van Cappellen, P., & Wang, Y. (1996). Cycling of iron and manganese in surface sediments: a general theory for the coupled transport and reaction of carbon, oxygen, nitrogen, sulfur, iron and manganese. *American Journal of Science*, *296*(March), 197–243.

Żygadłowska, O. M., Venetz, J., Klomp, R., Lenstra, W. K., Van Helmond, N. A. G. M., Röckmann, T., Wallenius, A. J., Dalcin Martins, P., Veraart, A. J., Jetten, M. S. M., & Slomp, C. P. (2023). Pathways of methane removal in the sediment and water column of a seasonally anoxic eutrophic marine basin. *Frontiers in Marine Science*, *January*, 1–15. https://doi.org/10.3389/fmars.2023.1085728